The study of passive film's resistivity distribution to crystalline Fe-based pseudo high entropy alloys: The use of measurement model and Cole-Cole regression

Weverson C Batalha, Alberto M Jorge Junior, Marc Mantel, Yannick Champion, Virginie Roche

Corrosion science 2024

The study of passive film's resistivity distribution to crystalline Fe-based pseudo high entropy alloys: The use of measurement model and Cole-Cole regression

Weverson C. Batalha [a,*], Alberto M. Jorge Junior [a,b,c], Marc Mantel [b], Yannick Champion [b], Virginie Roche [a,*]

[a] Univ. Grenoble Alpes, Univ. Savoie Mont Blanc, CNRS, Grenoble INP, Institute of Engineering and Management Univ. Grenoble Alpes, LEPMI, Grenoble 38000, France
[b] Univ. Grenoble Alpes, Univ. Savoie Mont Blanc, CNRS, Grenoble INP, Institute of Engineering and Management Univ. Grenoble Alpes, SIMAP, Grenoble 38000, France
[c] Graduate Program of Materials Science and Engineering, Federal University of São Carlos, Brazil

A B S T R A C T

In this work, for the first time, passive film formation on two newly developed pseudo high entropy alloys ($Fe_{61}Cr_{11}Mo_8Nb_4B_{16}$ and $Fe_{61}Cr_{11}Mo_8Ni_4B_{16}$) was deeply investigated by using combined XPS and EIS techniques. Amorphous and crystalized samples (ribbons) were tested in a 0.6 M NaCl solution. The Power Law model was the most appropriate to describe part of the data, and a passive film's physical properties, such as resistivity and capacitance were determined. The XPS analysis revealed that a thin oxide layer covered all samples and that samples' annealing decreased the amount of protective elements in the oxide layer, depleting corrosion properties.

1. Introduction

Seawater is a highly corrosive environment that covers about 70% of Earth's surface. It poses a significant challenge for structural materials, such as stainless steels (SSs), which are usually the preferred choice due to their cost-effectiveness in such demanding applications. Although these materials exhibit robust corrosion resistance by forming a protective oxide film, pitting corrosion in the presence of this corrosive media remains a significant concern [1]. Despite their many advantages, stainless steels are not exceptionally wear-resistant [2,3]. In addition, they are prone to a phenomenon known as sensitization when exposed to temperatures ranging from 550 °C to 800 °C. Sensitization occurs when chromium in the steel reacts with carbon or nitrogen, forming chromium carbides or nitrides at the grain boundaries. This process depletes the chromium from the steel, which reduces its corrosion resistance and makes it more susceptible to intergranular corrosion. Sensitization is a significant problem in stainless steel welding, and it can also occur during high-temperature processing or exposure to high temperatures for extended periods [4].

The above context highlights the need to find practical solutions for the reported issues. Fe-based bulk metallic glasses (BMGs) possess remarkable tribological and electrochemical properties, which make them a promising alternative for applications that require corrosion and wear resistance. However, it is worth noting that achieving a good balance between both properties remains a challenging task [5]. Furthermore, the application of BMGs is often limited by their brittleness and small critical size [6–8]. Despite these limitations, the possibility of producing coatings from these alloys to avoid such weaknesses has been gaining attention, particularly in the oil and gas industry [9–11]. Such coatings can be produced even from commercial precursors, which makes the process more feasible. BMG coatings offer numerous advantages, including improved wear and corrosion resistance, reduced friction, and enhanced mechanical properties.

Although the amorphous structure of Fe-based alloys is desired, crystallization can occur even when the material is in use, especially in a harsh environment [12]. The effect of crystallization on corrosion resistance depends directly on the phases and microstructures generated after crystallization [13]. Thus, understanding the crystallization path is extremely important. In the first precipitation stages, precipitates are formed with a similar composition to the matrix without significant depletion and low impact on corrosion properties. However, further stages of precipitation and grain coarsening may generate defects and a

* Corresponding authors.
E-mail addresses: weverson.capute-batalha@grenoble-inp.fr (W.C. Batalha), virginie.roche@lepmi.grenoble-inp.fr (V. Roche).

https://doi.org/10.1016/j.corsci.2024.111905
February 2024

lack of protective elements to form the protective film, causing a decrease in corrosion resistance [14,15]. As clarified in more detail in [16], the alloys studied in this work follow the rules proposed in [17, 18], being classified as pseudo-high entropy (PHE) amorphous alloys. Only two systems were reported in the literature [19,20], reinforcing the importance of a deeper understanding of these alloys' behavior.

One of the reasons for the outstanding corrosion behavior is the formation of a passive layer at the metal surface, often associated with the presence of Cr^{3+} species. In their work, Zhang et al. [21] highlighted the enhancement of protectiveness related to increased Nb content. Nb promotes repassivation. Adding B increases the corrosion resistance of Fe-Cr-based alloys [22]. Although some authors associate B atoms with passive film structure change, enhancing its protectiveness [23], it remains controversial. On the other hand, Mo is widely acknowledged as beneficial for corrosion resistance because it enriches and stabilizes Cr in the oxide layer through the presence of Mo^{6+} [24,25]. By forming austenite, Ni significantly enhances the corrosion resistance of crystalline alloys in chloride environments [26]. XPS has been successfully used to understand the film's passive structure [27–29] and was applied in this work towards the same purpose. However, thin oxide film formation is not wholly understood for multicomponent alloys.

Electrochemical Impedance Spectroscopy (EIS) has been successfully applied in the past few years to understand corrosion mechanisms involved in a system. By employing EIS, valuable insights concerning the dielectric properties of the electrodes can be obtained [30–32]. In their study, Tribollet et al. [28] introduced various models to describe an oxide layer as dielectric. Specifically, they proposed the Young and power-law models, which consider the passive film's resistivity changes relative to the distance from the sample surface. The power law model has been applied to characterize oxides on ASTM A416 steels [33], stainless steels, aluminum alloys [30], and magnesium alloys [34], allowing one to derive physical parameters, such as resistivity, as well as capacitance, hence the thickness of the passive layer.

In this work, we report using the power law model to characterize PHEs for the first time in the literature. This modeling was also confronted with the data regressed by Measurement Model (MM) software proposed by Orazem et al. [35,36] deconvoluting the interfaces in several Voigt circuits. The measurement model was initially created in the early 1990 s to quantify the error structure of electrochemical impedance spectroscopy measurements. It enables the extraction of capacitance, ohmic resistance, and polarization resistance values from impedance data. We also proposed to check the capacitance values using the Cole-Cole representation. The Cole-Cole representation has previously been used to obtain the capacitance of electrochemical systems [37,38]. As far as we know, such a study on PHE enables us to have a detailed comprehension of the mechanisms at the interface, and the formation of the passive film has never been reported in the literature. At first, investigations were performed on ribbon samples to yield a fully amorphous structure and better control the devitrification process. Earlier work has shown the impact of crystallization on corrosion and mechanical properties for these compositions [16]. Two novel PHEs were proposed: $Fe_{61}Cr_{11}Mo_8Nb_4B_{16}$ and $Fe_{61}Cr_{11}Mo_8Ni_4B_{16}$. Thus, the objective of this work is, by using a combination of two powerful techniques, EIS and XPS, to contribute to understanding the passive film formation of those complex alloys and contribute to developing a "database" within the literature concerning these new PHE alloys.

2. Materials and methods

2.1. Samples production and microstructural characterization

Ribbons with a 45 μm-thickness and 2 mm wide were produced from the ingots by melt spinning in a copper wheel. High pure elements were used, Fe 99.98%, Cr 99.99%, Mo 99.95%, Nb 99,8%, Ni 99.9%, and B 99.7%. The chamber was evacuated to reach 10^{-4} mbar and filled with Ar to obtain an ejection pressure of 200 mbar. A 45 m s^{-1} surface speed was applied. Ribbons were heat-treated in an electric furnace under Ar flow for controlled crystallization to avoid samples' oxidation. Four target temperatures were chosen for each composition based on differential scanning calorimetry (DSC) analysis: 640 °C, 720 °C, 810 °C, and 1000 °C for FeCrMoNbB, and 570 °C, 690 °C, 820 °C, and 1000 °C for FeCrMoNiB.

X-ray diffraction (XRD) analysis was conducted using the Bruker D8 Advanced equipment with Cu-Kα radiation, from 20 to 90° (2° min^{-1} of scan step) to characterize phase formation. Transmission (TEM) and scanning transmission electron microscopy (STEM) analyses were carried out using an FEI Tecnai G2F20 field emission gun (FEG) instrument at an acceleration voltage of 200 kV. The ribbon underwent thinning through ion milling in the Gatan PIPS 691 system. More details concerning sample production and characterization can be found in [16].

2.2. X-ray photoelectron Spectroscopy (XPS) characterization

X-ray photoelectron Spectroscopy (XPS) was performed after 2 h of immersion of the ribbons into the electrolyte. A Thermo Scientific K-alpha spectrometer with a monochromated Al X-ray source ($h\nu$ =1486.6 eV; spot size 400 μm) was employed. Pass energies of 30 and 100 eV were used to record the core level and the survey spectra, respectively. All spectra were acquired using an electron flood gun to compensate for possible positive charge accumulation during measurements. The obtained spectra were deconvoluted and fitted using Thermo Scientific Advantage Software. The C-C/C-H contribution of C1s spectra was fixed at 285.0 eV. The sensitivity factors of each element were used to calculate the percentage of each element in the oxide layer [39].

2.3. Electrochemical measurements

A three-electrode cell set-up was used with a Gamry Ref 600+ potentiostat for corrosion tests. The ribbon was used as the working electrode (WE). The exposed area was 0.3 cm^2. The reference electrode was a saturated calomel electrode (SCE), and a Platinum (Pt) grid was used as a counter-electrode. A platinum wire connected to a capacitor of 1 μF was connected in parallel with the reference electrode to avoid artifacts in high-frequency measurement. A chloride-rich environment (concentration of Cl^- equivalent to seawater) was prepared using demineralized water and 35 g L^{-1} of high-purity NaCl, with a natural pH of 5.5. The tests were performed at room temperature (25 °C). The experiment consisted of two hours of open circuit potential (OCP) to allow interface stabilization, followed by EIS spectra recorded from 0.02 Hz to 100 kHz. After an additional 20 minutes of OCP, potentiodynamic polarization measurements were performed from −30 mV to 1.2 V, with a scan rate of 1 mV s^{-1}. Data obtained from EIS were regressed using the Measurement Model software developed by Watson and Orazem to identify stochastic error structures [35,36]. The data were then modelized using SIMAD software developed at the Laboratoire Interfaces et Systèmes Electrochimiques (LISE) at Pierre et Marie Curie University (UPMC). Tests were performed at least three times to ensure reproducibility. Following the corrosion tests, the surface of the samples was analyzed using scanning electron microscopy (SEM) and energy-dispersive X-ray spectroscopy (EDX). The analysis was conducted using a FEG ZEISS Ultra 55 SEM equipment coupled with a SDD BRUKER AXS - 30 mm^2 detector for EDX microanalysis.

3. Results and discussion

3.1. Microstructural characterization

A thorough examination of the microstructure of the alloys investigated in this study was conducted using DSC, XRD, SEM, and TEM techniques. The detailed results and related discussion are in a previous publication [16].

The X-ray pattern in Fig. S1 (supplementary material) illustrates

phases' precipitation during the devitrification process of both alloys. As one may observe, the crystallization sequence of the Nb-containing PHE alloy can be summarized in: [am] → [remaining amorphous (am') + bcc] → [remaining amorphous (am″) + bcc] → [remaining amorphous (am‴) + bcc + bcc'] → [bcc' + boride']. Similarly, for the Ni-containing alloy, the sequence was [am] → [remaining amorphous (am') + bcc] → [remaining amorphous (am″) + bcc + boride''] → [fcc + boride' + boride"] → [bcc + boride'].

Here, am', am'', and am''' denote the remaining amorphous (am) phases after each heat treatment, with different compositions/structures than the preceding ones. Bcc represents the $Fe_{0.69}Cr_{0.25}Mo_{0.06}$ bcc-phase. This phase is claimed to form with minimal diffusion, exhibiting a chemical composition similar to the matrix, typical for PHE amorphous alloys [40]. Thus, it should maintain the corrosion properties of the amorphous phase. Bcc' is the $(Fe,Cr)_{0.875}Mo_{0.125}$ bcc phase, fcc is the $(Fe,Cr)_{0.80}Ni_{0.2}$ austenitic-type phase, boride' is the Mo_2FeB_2 (M_3B_2) boride, and boride'' is the Fe_3B boride. Different proportions of metallic elements (M = Fe, Cr, Mo, Nb) can be present in these borides. These crystallization sequences are anticipated for PHE amorphous alloys. As temperature rises, the amorphous percentage decreases, increasing heterogeneity and defects on the surface, hence, in the oxide film.

TEM analysis was performed for a better understanding of phase formation. Results of dark field images and diffraction patterns are presented in Fig. S2 (A-E) for Nb-containing composition and (F-J) for Ni-containing composition. In summary, the TEM image sequence shows how the amorphous ribbon undergoes devitrification in both cases. The process progresses through the formation of nanometric precipitates of the phases observed by XRD until they reach a completely crystalline structure. Images E and J depict the samples containing Nb and Ni, respectively. The alloy containing Ni undergoes the final crystallization stage at a lower temperature of around 800 °C than the sample containing Nb. As a result, the formed phases in the Ni-containing alloy coarsen between 800 °C and 1000 °C.

On the other hand, for the Nb-containing sample, new phases precipitate at 1000 °C. The diffraction patterns support the images, transitioning from the mere presence of the diffraction ring to the presence of multiple spots corresponding to the presence of the phases. The images primarily depict the transition from an amorphous and homogeneous structure to a complex and heterogeneous structure, which can directly impact the formation of the passive film and the corrosion properties of the alloy.

3.2. Open circuit potential

The variation of corrosion potential (E_{corr}) with time of the amorphous and heat-treated ribbons is shown in Fig. 1 for both compositions. The curves show, for the Nb-containing samples, that increasing heat treatment temperature, i.e., reducing the percentage of the amorphous phase, leads to more active corrosion potentials from around 0.02 V vs SCE for the as-spun sample to around −0.4 V vs SCE for samples heat treated at 1000 °C. In addition, FeCrMoNbB samples heat-treated at a temperature superior to 800 °C showed potential fluctuation that can be associated with constant consumption/reconstruction of the passive film. The inset figure in Fig. 1(a) shows the surface of a sample (Nb-containing ribbon annealed at 1000 °C) before immersion. It can be noted that the surface is heterogeneous due to the presence of precipitates. This non-uniformity of the film, i.e., a film that partially covers the surface, is inevitable and can lead to lower corrosion resistance or even initiation of localized corrosion due to defects in the protective film [41,42]. For the other samples, the potential remained stable with the increase of immersion time, indicating a stable surface condition. In the Ni-containing samples shown in (b), the potential remained steady over the immersion time, regardless of the heat treatment of the samples. One may observe a very similar potential value for the samples annealed up to 800 °C. After that, a drop of about 300 mV in the potential is observed. As spun Ni-containing samples exhibit lower corrosion potential compared to Nb-containing ones.

3.3. Potentiodynamic polarization curves

Fig. 2 shows the polarization curves for both compositions in a 35 g L^{-1} NaCl solution in the amorphous condition and after four annealing treatments. Except for samples heat-treated over 800°C, where a clear Tafel region was observed, as expected, no Tafel region was identified in other conditions where samples already started passivated during testing. Thus, for these conditions, $i_{0.2Vvs.Ecorr}$ (a region sufficiently far from E_{corr}) was considered the same as the corrosion

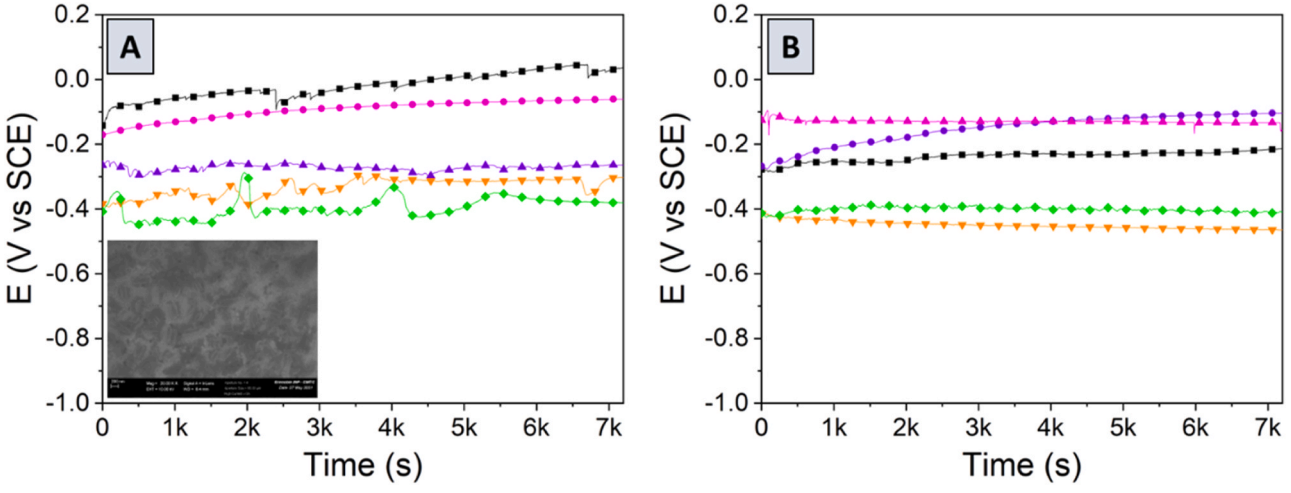

Fig. 1. – Open-circuit potential evolution of the as-spun and annealed ribbons as a function of time in a 35 g L^{-1} NaCl solution at 25 °C (a) FeCrMoNbB alloy (■) as-spun, (●) 640 °C, (▲) 720 °C, (▼) 810 °C, (◆) 1000 °C and (b) FeCrMoNiB alloy (■) as-spun, (●) 570 °C, (▲) 690 °C, (▼) 820 °C, (◆) 1000 °C. The inset image in (a) corresponds to an SEM image of the surface of the ribbon heat treated at 1000 °C (Nb-containing alloy).

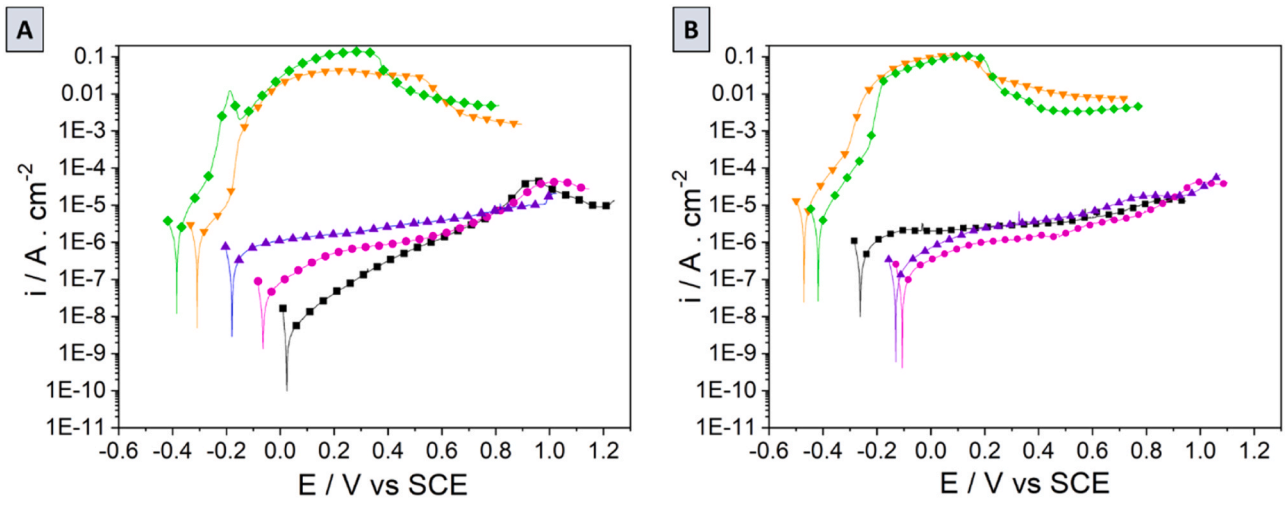

Fig. 2. Potentiodynamic polarization curves of the amorphous and annealed ribbons performed in a 0.6 M NaCl solution (35 g L^{-1}) at 25 °C from −0.03 to 1.2 versus E_{corr}. (a) FeCrMoNbB alloy (■) as-spun, (●) 640 °C, (▲) 720 °C, (▼) 810 °C, (◆) 1000 °C, and (b) FeCrMoNiB alloy (■) as-spun, (●) 570 °C, (▲) 690 °C, (▼) 820 °C, (◆) 1000 °C.

current (i_{corr}). The Tafel extrapolation was used for other conditions to get the i_{corr} values. The $i_{0.2Vvs.Ecorr}$ and E_{corr} values extracted from polarization curves are shown in Table 1. Heating temperatures were chosen based on crystallization peaks identified on DSC curves (refer to [16]). In this work, the presence of other ions such as HCO_3^-, SO_4^{2-}, K^+, and Mg^{2+}, as well as organic components/microorganisms in seawater, was not considered, even if the authors are aware that it may have a significant impact on the corrosion behavior, accelerating or even mitigating corrosion phenomena [43,44].

For the Nb-containing alloy, corrosion resistance degrades right after the first heat treatment, observing in terms of corrosion current density that reduces in more than one decade and corrosion potential, i.e., decreasing amorphous fraction leads to depletion of corrosion resistance. This behavior can be associated with many factors: an increase of heterogeneities on the surface, accompanied by a reduction of amorphous content, precipitation of borides, and other phases containing protective elements, such as Cr and Nb, that are no longer available to form the passive film. Similar behavior was observed in the literature for Fe-based metallic glass alloys [15,45–48]. The superior corrosion resistance of the amorphous materials is often associated with the absence of chemical and physical heterogeneities. A single homogeneous phase forms these materials. Once they have a sufficient concentration of corrosion-resistant elements, they show higher corrosion resistance than crystalline metallic materials [49]. However, even if the corrosion current increased more than one decade after the two first heat treatments, from around 10 nA cm^{-2} to 0.7 μA cm^{-2}, the beginning of crystallization does not seem to affect the presence of the passivation plateau that extends for more than 900 mV (vs. SCE) with a passive current density of the order 10^{-6} A cm^{-2}. As expected, no clear Tafel region was identified.

The corrosion properties significantly degraded for samples heat-treated above 800°C. Ecorr values were −303 mV and −377 mV and $i_{0.2Vvs.Ecorr}$ values were around 1.4 μA cm^{-2} and 3 μA cm^{-2} for 810°C and 1000°C samples, respectively. Despite relatively low corrosion currents in the order of 10^{-6} A cm^{-2}, a significant increase in the current after the corrosion potential was observed, and no passivation plateau was noted in these cases where generalized corrosion occurs.

Fig. 2(b) shows the potentiodynamic polarization curves for the Ni-containing composition. Despite having lower corrosion resistance than the Nb-containing alloy, the as-spun and devitrified samples up to 690 °C Ni-containing alloy show excellent properties, revealing similar values of $i_{0.2Vvs.Ecorr}$ around 10^{-6} A cm^{-2}. The corrosion potential value was even better for the sample heat-treated at 690 °C than the amorphous one. An extensive passivation plateau was also observed for these samples. Similar to the case shown in (a) for the Nb-containing alloy, the samples heat-treated at temperatures above 800 °C suffered generalized corrosion. However, the corrosion properties of the Ni-containing alloy were less sensitive to the devitrification process in the solution used in this study. Up to 690 °C, a very similar behavior with very close values of $i_{0.2Vvs.Ecorr}$ and corrosion potential was found for the samples. It is essential to highlight that the pitting corrosion phenomenon, quite often observed for amorphous Fe-based alloys in the literature [8,21,50,51], was not observed for the two compositions studied in this work, which renders the alloys more attractive for several applications.

The cathodic polarization response was also measured for the sample heat-treated at 810 °C (Nb) and 820 °C (Ni). A plateau is observed in both cases with the corresponding current of 10^{-4} A cm^{-2}. The presence of this plateau indicates that the reduction of dissolved oxygen limits the reaction. We can infer that at E_{corr}, the reaction is limited by the cathodic reaction.

Fig. 3 shows SEM images of ribbons that underwent potentiodynamic polarization experiments to enhance our understanding of their corrosion behavior. The images depict the FeCrMoNbB alloy (A-D) and the

Table 1
Electrochemical properties were obtained from potentiodynamic polarization curves in slightly acid media (pH5.5) in a 0.6 M NaCl solution, based on the results of at least three experiments to ensure reproducibility. $I_{corr} = i_{0.2Vvs.Ecorr}$ for conditions treated at temperatures below 800 °C.

FeCrMoNbB			**FeCrMoNiB**		
Sample	E_{corr} mV vs. SCE	i_{corr} μA cm^{-2}	Sample	E_{corr} mV vs. SCE	I_{corr} μA cm^{-2}
AS	24 ± 4	5.4E-2 ± 0.6E-2	AS	-262 ± 18	2.1 ± 0.6
640	-58 ± 3	0.33 ± 0.08	570	-105 ± 12	0.6 ± 0.6
720	-177 ± 19	1.2 ± 0.2	690	-129 ± 15	1.0 ± 1.1
810	-303 ± 32	1.4± 0.5	820	-469 ± 24	9.0 ± 1.3
1000	-377 ± 19	3.0 ± 1.7	1000	-419 ± 19	6.7 ± 0.8

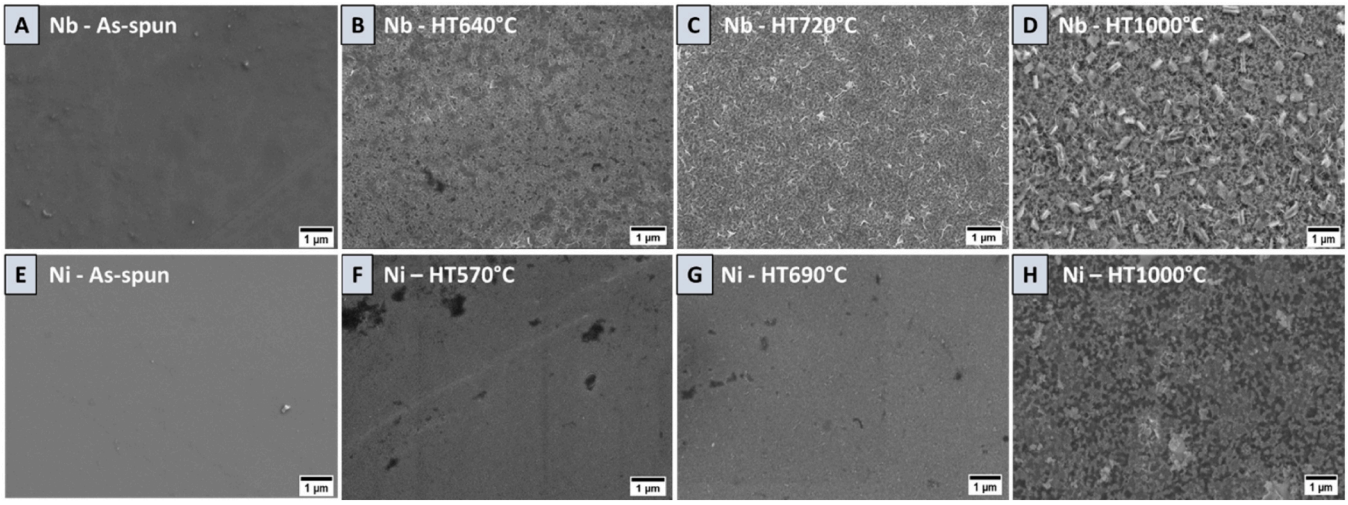

Fig. 3. – SEM images of the ribbons after potentiodynamic polarization test in a 0.6 M NaCl solution at 25 °C of FeCrMoNbB alloy ribbon (A-D) and FeCrMoNiB alloy ribbon (E-H).

FeCrMoNiB alloy (E-H). Table 2 presents the results of EDX analysis for both samples, considering the presence of oxygen and the absence of B. The images confirm that no pitting occurred in samples showing a passive plateau in the potentiodynamic curves: A-C for the alloy with Nb and E-G for the Ni-containing alloy. Corrosion products have formed on the surface and can be seen in the images. Images D and F show a fully crystallized ribbon after corrosion tests, confirming the occurrence of generalized corrosion. The images also clearly show resistant precipitates in the matrix that the corrosion process has partially consumed.

According to the EDX results in Table 2, the percentage of surface elements (except B) after the first and second heat treatments is comparable to the proposed theoretical composition. However, a significant increase in oxygen levels is observed for the sample that underwent generalized corrosion, possibly due to the formation of corrosion products. Moreover, there is a decrease in the Fe content, accompanied by increased protective elements such as Cr, Mo, and Nb. The XRD analysis (Fig. S1) indicates that these elements will form precipitates, leading to their deficiency in the matrix, which becomes more prone to corrosion. The absence of Ni in the sample heat-treated at 1000 °C, which experienced generalized corrosion, may indicate that this element formed an fcc or bcc phase (Fig. S1) that dissolved in the solution.

After immersing the sample for 2 hours, EIS and XPS analysis were performed to better understand of the structure and composition of the passive film. The results will be discussed below.

3.4. Electrochemical impedance spectroscopy (EIS)

Figs. 4(a) and 5(a) display the Nyquist plot for both compositions' as-spun and annealed samples. Typical capacitive-like response represented by inclined lines or semi-circles was identified for all samples, suggesting the presence of an oxide layer at the interface, whatever the composition and annealing, that limits the reactions between the substrate and the electrolyte. Qualitatively for the Nb-containing alloy, increasing the heating treatment temperature reduces the diameter of the semi-circle, suggesting lower protectiveness of the oxide layer. Nyquist plot for the Ni-containing composition also consists of semi-circles. However, unlike the case of the Nb-containing alloy, a subtle difference between the behavior of the as-spun sample and after heat treatment at 690 °C can be noted. The sample treated at 570 °C exhibits superior performance. The Bode plot is presented in Figs. 4(b) and 5(b) for Nb and Ni-containing composition, respectively. For the Nb-containing alloy, the low frequencies impedance modulus $|Z|$ decreased from around 370 kΩ cm^{-2} (as-spun sample) to 7 kΩ cm^{-2} when the temperature increased (sample heat treated at 1000 °C), meaning higher corrosion resistance for the as-spun sample, corroborating potentiodynamic polarization curves results. A slight difference is observed between the as-spun sample and the samples after the first two stages of heat treatment for the Ni-containing alloy. The values found were around 50 kΩ cm^{-2}, much lower than the $|Z|$ obtained for the as-spun sample of the Nb-containing alloy.

A bode plot can help recognize the number of time constants. However, an ohmic resistance (R_e) or impedance can mask some phenomena in high frequencies. This so-called ohmic resistance/impedance is related to a non-uniform current distribution associated with the geometry of the electrode and the sample holder [52,53].

Figure S3 (supplementary material) shows a zoom of the high-frequency part evidencing the ohmic impedance effect, which makes it challenging to identify a value for the electrolyte resistance R_e. In this work, after correcting the Bode diagram by ohmic impedance, it was observed that there was no significant gain of information regarding the properties of the passive film. Therefore, only the correction for the electrolyte resistance R_e (determined by MM) was considered, neglecting the high-frequency part (from 100 Hz) for the impedance data fitting.

Thus, the correction of impedance modulus and phase angle is calculated by Eqs. 1 and 2, respectively [54],

$$|Z|_{corrected} = \sqrt{(Z_r - R_e)^2 + Z_i^2}, \quad (1)$$

Table 2 –
General composition of the surface obtained by EDX analysis (B not included).

Nb	Fe	Cr	Mo	Nb	O	Ni	Fe	Cr	Mo	Ni	O
AS	71.7	12.6	8.4	4.2	3.1	**AS**	70.9	13.0	9.2	4.2	2.7
HT640	65.6	11.3	7.6	4.3	11.2	**HT570**	69.3	13.1	8.5	4.2	5.1
HT720	53.2	12.5	6.4	4.2	23.7	**HT690**	73.5	12.4	7.6	3.9	2.6
HT1000	15.9	15.9	17.3	9.5	41.4	**HT1000**	28.9	25.6	26.8	0	18.7

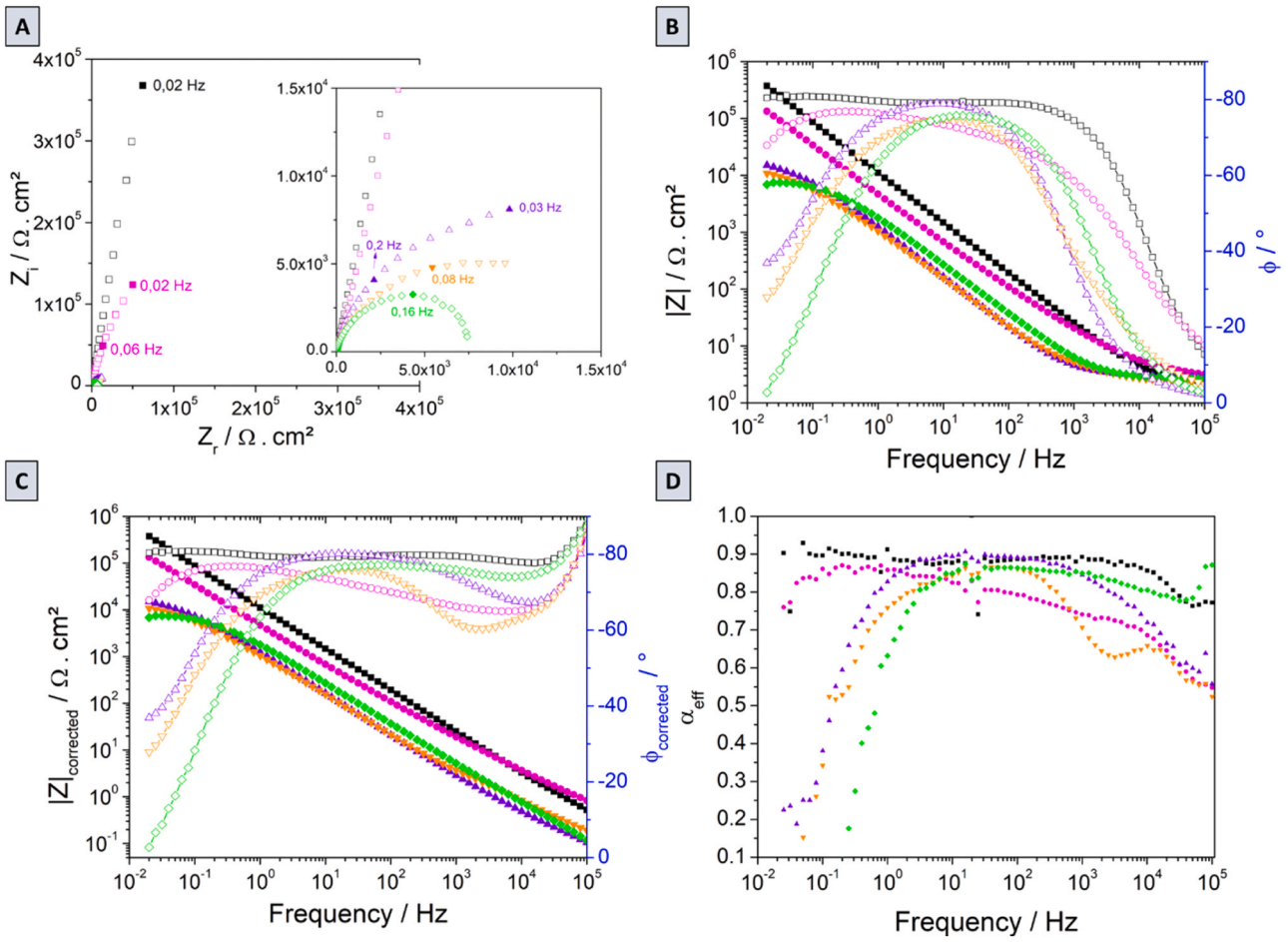

Fig. 4. EIS results obtained after 2 hours of immersion in a 0.6 M NaCl solution for the FeCrMoNbB composition. In (a) Nyquist plot for the experimental and fitted results; (b) Bode-plot diagram; (c) Corrected bode-plot; and (d) α_{eff} versus frequency. The symbol (■) corresponds to the as-spun, (●) 640 °C, (▲) 720 °C, (▼) 810 °C, and (◆)1000 °C.

$$\Phi_{corrected} = \tan^{-1}\left(\frac{Z_i}{Z_r - R_e}\right), \tag{2}$$

Different data treatments and representations could be done to identify better the number of time constants involved. In this sense, we chose to plot α_{eff} [55],

$$\alpha_{eff} = \left|\frac{dlog|Z_i(f)|}{dlogf}\right|, \tag{3}$$

The calculus considers the derivative of the imaginary part (Z_i) on a log-log scale.

Figs. 4(d) and 5(d) show the variation of α_{eff} with frequency for the Nb-containing and Ni-containing composition, respectively. A plateau over the frequency range typically suggests a capacitive or pseudo-capacitive behavior (CPE). For the as-spun sample (Nb-containing composition), we observe a plateau extending over the entire frequency range, which can be associated with only one CPE whose α parameter would be equal to 0.88. For the 720 °C thermally treated alloys, considering the medium frequency region, we observe only one plateau corresponding to a single time constant with alpha between 0.8 and 0.9 which supports the assumption that the CPE behavior valid at medium dominates the capacitive response. Whereas for the sample heated to 640 °C, the existence of one or more plateaus is unclear, and we observe a decrease of α value with increasing frequency (Fig. 4(b)). Sample heat treated at 810 °C shows two plateaus, one in middle frequency from around 5–200 Hz and another around 10^4 Hz. Furthermore, for the 1000 °C HT sample, we observe a plateau from 10 Hz. In all cases, in Figs. 4(c) and 5(c), the corrected bode plot shows a decrease of the α value from 10^2-10^3 Hz (10^4 Hz for the Nb-containing as-spun sample) which is associated with the influence of the ohmic impedance at high frequency.

The as-spun and heat-treated 690 °C Ni-containing alloy sample, similarly to the Nb-containing alloy, shows only a mid-frequency plateau ranging from 1 to 10^3 Hz, corresponding to a CPE behavior with an alpha of 0.92. The sample treated at 570 °C shows two well-defined time constants (one at low-frequency from 0.1 to 10 Hz, and a second one at mid-frequency from 10 to 10^3 Hz), with alpha of 0.85 and 0.78, respectively (Fig. 5(d)). This behavior should illustrate an intermediate interface state as the heating temperature is closer to the T_g. For the samples heated at 820 °C and 1000 °C, alpha decreased with the frequency (Fig. 5(c) and (d)) as observed typically for a reactive electrode [56].

For both compositions, we can already infer from this first approach that sample heat treated at temperatures lower than 800 °C shows capacitive behavior of the metal/ electrolyte interface with at least one CPE observed.

3.4.1. SIMAD simulation

The impedance of films showing CPE behavior was simulated using SIMAD software, assuming a non-ideal capacitive behavior related to resistivity distribution in the oxide layer simulated by the power law model reported for the first time in the literature for those alloys. Additionally, at frequencies below 10 Hz, the phase angle decreases for all the samples, corresponding to a faradaic impedance or an O_2-related diffusion phenomenon. Therefore, the discussion will further present a

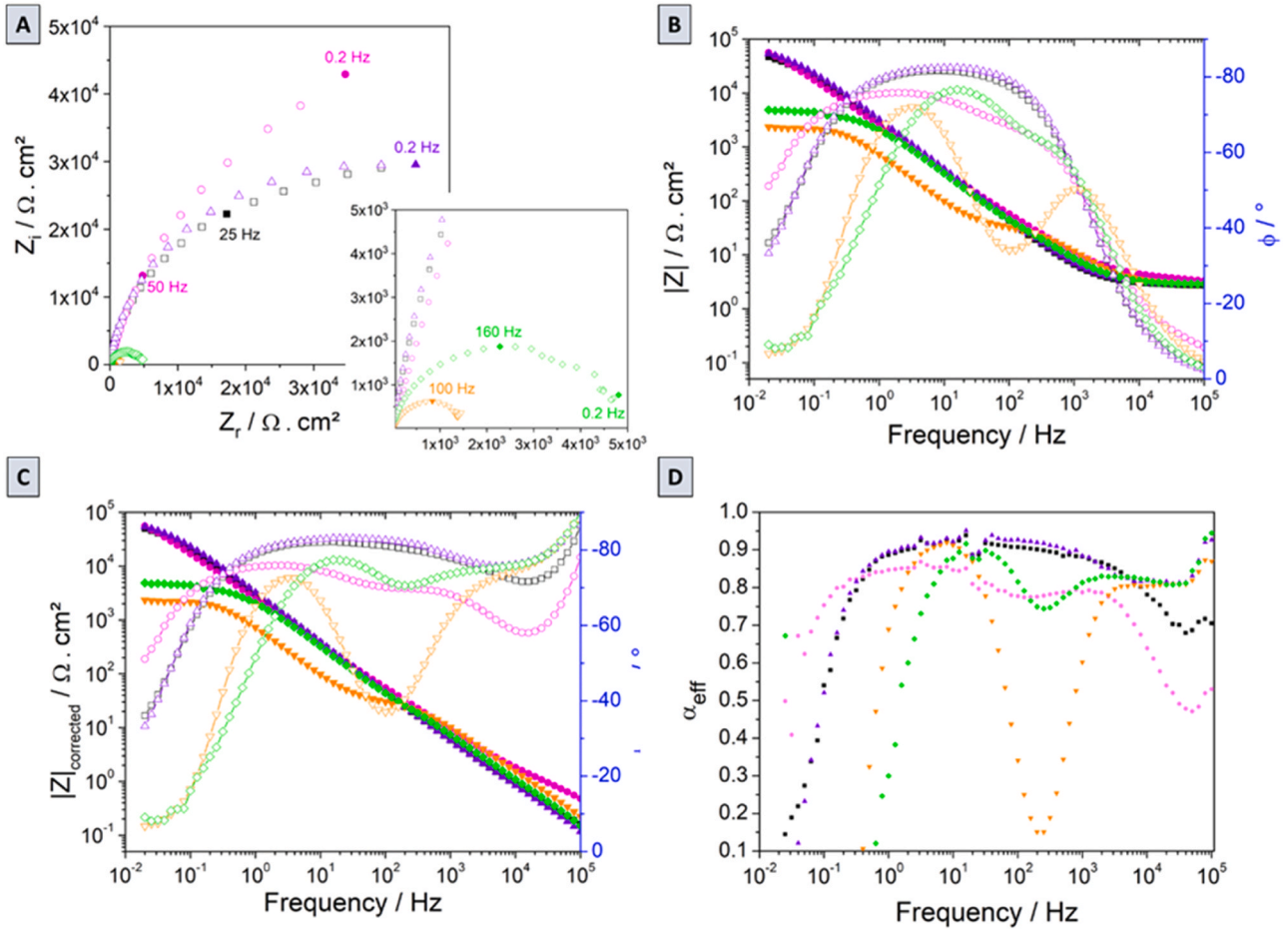

Fig. 5. - EIS results obtained after 2 hours of immersion in a 0.6 M NaCl solution for the FeCrMoNiB composition. In (a) Nyquist plot for the experimental and fitted results; (b) Bode-plot diagram; (c) Corrected bode-plot; (d) α_{eff} versus frequency. The symbol (■) corresponds to the as-spun, (●) 570 °C, (▲) 690 °C, (▼) 820 °C, and (◆) 1000 °C.

schematic representation of the interface.

In this case, the impedance of the film can be described as [57,58]

$$Z_{film}(\omega) = g\frac{\delta\rho_{\delta}^{1-\alpha}}{(\rho_0{}^{-1} + j\omega\varepsilon\varepsilon_0)^{\alpha}}, \quad (4)$$

Where ρ_0 is the resistivity at the metal/oxide interface, ρ_δ is the resistivity at the oxide/electrolyte interface, ω is the pulsation, and j is the imaginary number ($j^2 = -1$).

The function g is given by

$$g = 1 + 2.88(1-\alpha)^{2.375}, \quad (5)$$

The CPE parameter Q can be obtained by the graphical method (Fig. S5). There are several ways to obtain the α parameter, such as directly after regressing the data via SIMAD. It can also be obtained graphically by plotting the relationship between $|Z_i|$ and frequency (Fig. S6) or via the plot of α_{eff}.

There is also a relationship between these parameters and ε, ρ_δ, δ and the other CPE parameter α, given by [58]

$$Q = \frac{(\varepsilon\varepsilon_0)^{\alpha}}{g\delta\rho_{\delta}^{1-\alpha}}, \quad (6)$$

Hence the parameters Q and α obtained above are used to estimate the value of ρ_δ, but we need to get the thickness value from the capacitance. The capacitance can be obtained using the measurement model or Cole-Cole representation.

3.4.2. *Cole-Cole diagram*

Cole-Cole diagrams [36,38] were employed to obtain more information about the oxide layer and the capacitance values. It consists of transforming the impedance spectrum into a capacitance spectrum (Eq. 7). The value of oxide capacitance corresponds to the extrapolation at the infinite frequency of the complex capacitance.

$$C^* = \frac{1}{j\omega(Z - R_e)}, \quad (7)$$

However, this method requires precise estimation of the ohmic resistance Re, which can be challenging. The real part can be calculated by using Eq. 8

$$C_r = \frac{-Zimg}{2\pi fx\left(Zimg^2 + Zr^2_{\text{corrected by Re}}\right)}, \quad (8)$$

And the imaginary part is given by Eq. 9

$$-C_{img} = \frac{Zr_{\text{corrected by Re}}}{2\pi fx\left(Zimg^2 + Zr^2_{\text{corrected by Re}}\right)}, \quad (9)$$

Once the capacitance value is determined by extrapolation to infinity of C_r, the thickness of the oxide layer can be calculated using Eq. 10, where $\varepsilon_0 = 8.85\times10^{-14}$ F cm^{-1} is the vacuum permittivity and $\varepsilon_r = 12$ is the material relative dielectric constant (typical value of Fe and Cr oxide layers [59]). In the case of layers composed of several oxides, estimating this value is challenging, varying between 10 and 100 depending on the material. Such considerable permittivity variation can lead to an

additional error in the capacitance estimation.

$$\delta_{Ox} = \frac{\varepsilon\varepsilon_0}{C_{Ox}}, \tag{10}$$

An example of a Cole-Cole graph used to estimate the thickness of the oxide layer for the as-spun sample of the Nb-containing alloy is shown in Fig. S4. The extrapolation of the domain of frequency correspondent to the CPE crosses the origin, as indicated by the straight line in Fig. S4. The method was applied to the two compositions studied for the samples that presented a passivation plateau related to the passive layer in the potentiodynamic curves shown in Fig. 2. The results are shown in Table 3.

The values found for the thickness of the oxide layer are between 0.8 and 5.6 nm, typical of a passive layer. Values in the range 1–10 nm are typically associated with the presence of a passive film. In addition, an increase in capacitance value may indicate the presence of a less-performing film that does not cover the entire surface [60].

3.4.3. Measurement model

The measurement model is another helpful tool, originally developed to determine the error structure of the data, that can be helpful to characterize the passive film. Agarwal et al. [61] proposed the fitting impedance data by adding sufficiently Voigt elements (R//C circuits) in series with an electrolyte resistance. Sequentially increasing the number of Voigt elements was done while ensuring that the 95.4% confidence interval for each regressed parameter does not encompass zero. The regression of the Voigt measurement model gives two essential pieces of information for passive film description, the electrolyte resistance and the capacitance. From the last, the thickness of the passive film can be estimated by Eq. 10, as already discussed. The error between the simulation and the measurement (χ) must be lower than 1%, characterizing a good fitting level, and it is given by

$$\chi^2 = \sum_{i=1}^{N_{dat}} \frac{\left(y_i - \sum_{k=1}^{N_p} P_k X_k(x_i)\right)^2}{\sigma_i^2}, \tag{11}$$

where P_k is N_p adjustable parameters; X_k (x_i) is a basic arbitrary function; x_i and y_i are experimental values, and σi is the standard deviation of the measured value.

The results for the regressed data for Nb and Ni-containing compositions are given in Tables 4 and 5, respectively.

The results found for the electrolyte resistance ($_{Re}$) are consistent with those estimated by the graphical analysis (through the Nyquist diagram). The capacitance values, hence the oxide film thickness values, are concordant with the values estimated by Cole-Cole. Typical of a passive layer, as expected from the analysis of the potentiodynamic curves presented in Fig. 2. Here, one must be aware that using several Voigt circuits to represent the interface appears to be perfectly acceptable, as the Cole-Cole method yields identical results. Even though substituting $_{Re}$ for Z_e in the Cole-Cole method may lead to an error, the hypothesis is reasonable since it still delivers comparable outcomes.

Finally, an expression of the capacitance of the oxide film dependent on the dielectric constant of the material that associates capacitance with resistivity at the interface film/electrolyte ρ_δ is given by

$$C_{film} = gQ(\rho_\delta \varepsilon\varepsilon_0)^{1-\alpha}, \tag{12}$$

The work aims to extract the most parameters that allow us to describe the oxide film formed on the surface of the studied alloys to see the impact of crystallization and composition on the film. The parameters obtained by regressing the data and those calculated using Eqs. 10–14 are presented in Tables 6 and 7 (Nb and Ni containing alloy, respectively). Calculating these parameters allows one to identify the nature of the film formed, confront what is physically expected, and compare the samples in terms of their resistivity profile.

The values found for ρ_0 and ρ_δ for both alloys are characteristic of insulators and semiconductors, respectively [57]. Since ρ_0 is the resistivity value at the metal/oxide interface, high values of this parameter may be associated with a high degree of surface protection of the material. For the Nb-containing alloy, it can be noticed that the resistivity value ρ_0 decreases by about one decade when the sample is heat-treated at 720 °C. This behavior is consistent with the results shown earlier, which point to a degradation of the corrosion properties with increasing temperature. Similar behavior is noted when comparing the as-spun samples of the two alloys studied. A lower resistivity value, of the order of 10^{12} Ω cm, was found for the case of the alloy containing Ni, a difference of one decade concerning the alloy containing Nb, as expected.

The values of film capacitance C_{film} calculated by Eq. 12 are concordant with those obtained by the Measurement Model and Cole-Cole. These values were used to estimate the thickness of the passive layer using Eq. 10. Values below 1 nm were found for all cases—typical values for a protective passive layer.

The error between the measurement and the simulation (χ) was around 1% or lower for all the samples, indicating a satisfactory fitting level. SIMAD software minimized the χ^2 given by Eq. 11. The values found for thickness are only approximations. A parameter that can be used to compare the samples is the resistivity value. The behavior at 640 °C (Nb) and 570 °C (Ni) is not fully understood. For both samples, the values found for capacitance (<10 μF) and thickness (about 5 nm) suggest the existence of a protective passive layer. However, for the 640

Table 3 –
Capacitance obtained from Cole-Cole (C_{cc}) diagram and calculated thickness (δ) of the oxide layer considering $\varepsilon = 12$.

Sample	Nb C_{cc} μF cm^{-2}	Nb δ_{cc} nm	Ni C_{cc} μF cm^{-2}	Ni δ_{cc} nm
As-spun	3.4	3.2	10.3	1.0
1st HT	1.9	5.6	3.4	3.1
2nd HT	13.6	0.8	13.5	0.8

Table 4
Results obtained by Measurement Model regression for the Nb-containing composition.

Parameter	As-spun	HT640°C	HT720°C
Re	2.22 ± 0.01	2.69 ± 0.02	2.83 ± 0.01
C_{MM} (μF cm^{-2})	2.89 ± 0.14	1.46 ± 0.06	13.64 ± 1.07
Voigt elements	10	10	12
χ^2	0.003	0.001	0.0001
δ[a] (nm)[a]	3.7	7.3	0.8

[a] *Calculated by using* Eq. 10.

Table 5
Results obtained by Measurement Model regression for the Ni-containing composition.

Parameter	As-spun	HT570°C	HT690°C
Re	2.69 ± 0.01	3.08 ± 0.01	2.89 ± 0.01
C_{MM} (μFcm^{-2})	10.95 ± 0.57	2.88 ± 1.6	13.75 ± 0.79
Voigt elements	9	10	9
χ^2	0.001	0.002	0.001
δ[a] (nm)[a]	1.0	3.7	0.8

[a] *Calculated using* Eq. 10.

Table 6
Results obtained by SIMAD regression for the Nb-containing composition.

Parameter	As-spun	HT 720°C
ρ_0 (Ω cm)	1.75 ×10^{13}	1.27 ×10^{12}
ρ_δ (Ω cm)	4.25 ×10^{7}	2.06 ×10^{2}
C_{film} (μF cm^{-2})	3.4	13.5
(Q,α) (μF s$^{\alpha-1}$)	17, 0.88	15, 0.89
δ_{film} (nm)	3.2	0.8
χ	0.83	0.49

Table 7
Results obtained by SIMAD regression for the Ni-containing composition.

Parameter	As-spun	HT 690°C
ρ_0 (Ω cm)	2.88×10^{12}	2.93×10^{12}
ρ_δ (Ω cm)	1.73×10^{3}	3.51×10^{5}
C_{film} (μF cm^{-2})	11	13.6
(Q,α) (μF $s^{\alpha-1}$)	67, 0.91	50, 0.92
δ_{film} (nm)	0.97	0.80
χ	0.99	1.07

°C sample, no plateau characteristic of a CPE was detected. Instead, a phase that decreases with frequency is observed (Fig. 4(c)). The two models proposed in the literature, the Power Law and Young Model, do not predict a decrease in the phase with frequency. In turn, the 570 °C sample showed two plateaus (Fig. 5(d)) with alphas of 0.85 and 0.78, at low (up to 20 Hz) and mid/high frequency (20–2000 Hz), respectively.

Interestingly, for both compositions, the samples heated at temperatures just above T_g (100 °C for the Nb-containing alloy and 70 °C for the Ni one) showed a different behavior compared to the other passive samples. Authors have associated improved corrosion properties with the relaxation process in the literature. Reducing the free volume induces the formation of a compact and hence more protective passive layer [62,63]. Nevertheless, this is observed for a temperature below T_g. Treatments above T_x resulting in crystallization are generally associated with a deterioration of the corrosion properties.

The resistivity profile calculated through the fitting data obtained in SIMAD is shown in Fig. 6. The difference observed between the resistivity profiles for the as-spun samples of both compositions can be associated with the compositional differences presented by the passive film.

The resistivity profile calculated through the fitting data obtained in SIMAD is presented in Fig. 6, based on the equation that describes the Power Law [64]:

$$\frac{\rho}{\rho_\delta} = \left(\frac{\rho_\delta}{\rho_0} + \left(1 - \frac{\rho_\delta}{\rho_0}\right)\xi^\gamma\right)^{-1}, \tag{13}$$

The fitting with SIMAD allowed estimating the resistivity values at the metal/oxide interface (ρ_0), the oxide/electrolyte interface (ρ_δ), and the resistivity profile through the oxide layer. After comparing the as-spun samples of both compositions, it was observed that the Nb-containing alloy has a higher value of ρ_0 (around 10^{13} Ω cm) compared to the Ni-containing alloy (one decade lower), confirming the belief that the Nb-containing alloy presents better corrosion resistance. When comparing the as-spun and heat-treated samples for both alloys, it was observed that the resistivity profile was consistent with the behavior observed through the potentiodynamic curves. In the case of the Nb-containing alloy, there was a decrease in the values of ρ_0 and ρ_δ with an increase in temperature. As for the Ni-containing alloy, after heat treatment at 690°C, the resistivity ρ_0 value remained similar, but the ρ_δ was superior for the heat-treated sample, consistent with the behavior

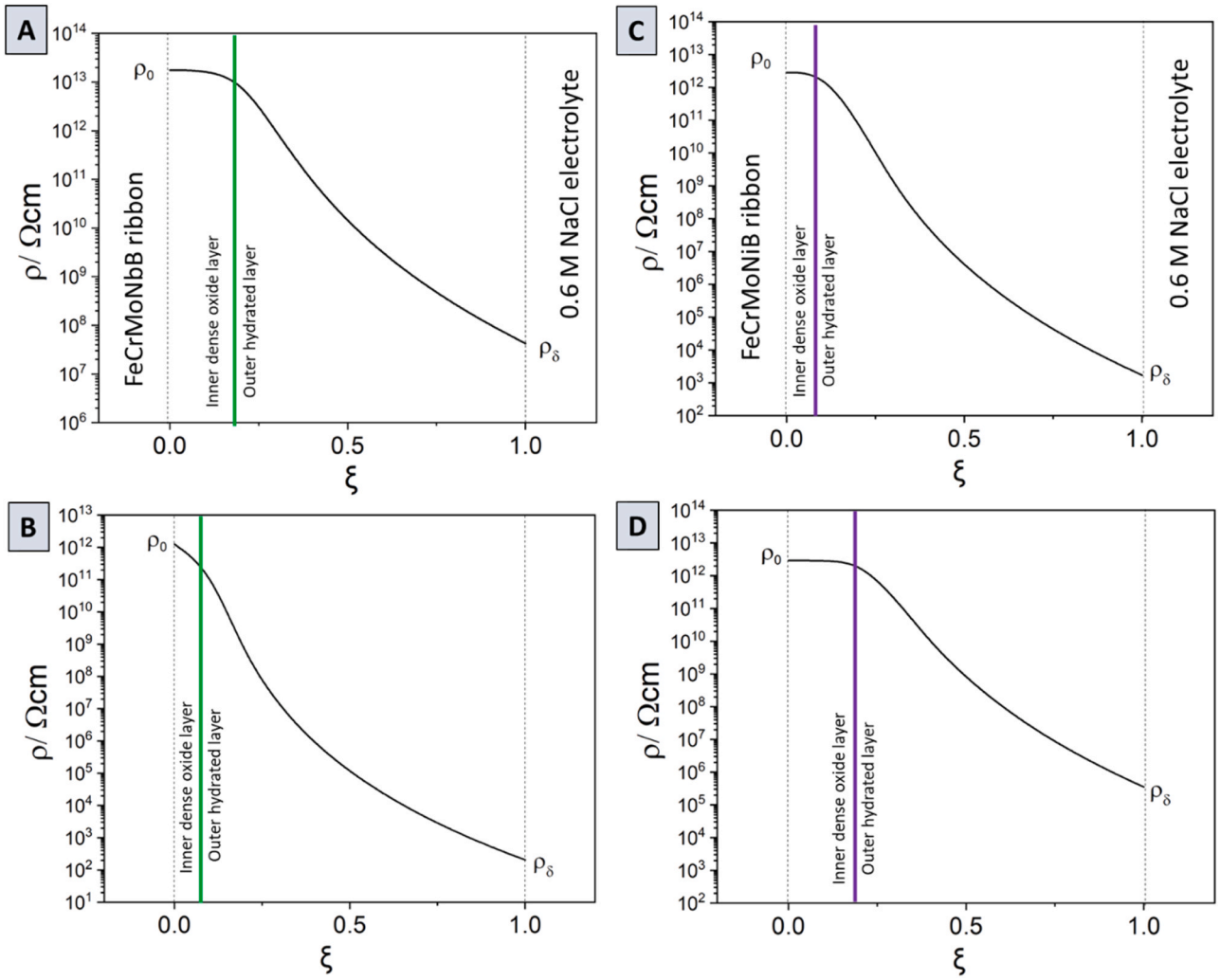

Fig. 6. - Resistivity profiles obtained from the fitted parameters for the (A) FeCrMoNbB as-spun sample, (B) FeCrMoNbB 720°C, (C) FeCrMoNiB as-spun, and (D) FeCrMoNiB 690°C. ρ is the resistivity obtained by applying the Pawer low and ξ is the dimensionless position ($\mathfrak{r}/\delta$).

observed by the potentiodynamic curves, which was similar, but slightly better for the heat-treated sample.

Based on the model presented by Marcelin et al. [65], the resistivity curves reveal two distinct domains. The first domain is characterized by a constant resistivity value, denoted as ρ0, at the alloy/passive film interface. Conversely, the second domain shows a decrease in resistivity toward the passive film/electrolyte interface, represented by ρδ. This bimodal distribution of resistivity is associated with the dual structure of the passive film, consisting of a dense inner oxide layer (such as Cr_2O_3) and an outer, more hydrated layer primarily composed of hydroxides.

XPS was employed primarily to gather qualitative information to understand better the passive film formed in these alloys. The results and related discussion are presented below.

3.5. X-ray photoelectron Spectroscopy (XPS) results

The oxides forming the passive film give essential information about the stability and protectiveness of the film. X-ray Photoelectron Spectroscopy technique was used in this study to comprehend, especially from a qualitative point of view, the formation of oxides that compose surface layers of as-spun and crystallized samples after exposing them to a chloride-rich solution for two hours. Employing this technique, we sought to identify the effect of devitrification on the oxide layer composition and correlate it with the behavior observed through the potentiodynamic properties obtained from the potentiodynamic polarization curves and EIS measurements.

General XPS spectra for both compositions in all conditions can be seen in Fig. S7 (supplementary materials). The fitted spectra for each alloy element present in the passive film for the amorphous ribbons are shown in Fig. 4 (Nb-containing composition) and Fig. 5 (Ni-containing composition). The $Fe2p_{3/2}$ spectra were decomposed into four peaks around 706.8 eV, 710.1 eV, 711.0 eV, 712.9 ± 0.2 eV, corresponding to Fe° metallic state, and FeO, Fe_2O_3, and FeOOH [27,66]. The $Cr2p_{3/2}$ spectra consist of three peaks. One peak around 574 eV that can be assigned to the electrons originated from Cr°, and peaks around 576.5 eV and 577.4 eV that correspond to Cr^{3+} and Cr^{6+} oxidic states [67,68]. In turn, Mo3d spectra are composed of two peaks originating from Mo° in the metallic state (228 eV and 231 eV), as well as two peaks for Mo^{4+} (228.4 and 231.2 eV) and Mo^{6+} oxidized state species (232.2 and 235.2 eV) [69]. Similar to Mo, Nb3d was decomposed into two peaks corresponding to Nb° (202.1 and 204.3 eV) and two peaks between 203.1 and 210.1, related to the presence of three different oxides, NbO, NbO_2, and Nb_2O_5 [70]. In the case of amorphous samples for both compositions, B1s spectra were found to be composed by a contribution of the pure element, B°, around 188 eV, and a contribution of B-O type oxides. However, for some of the crystallized samples, the presence of B_2O_3 could be detected with a peak around 193.4 eV [67,71]. Ni oxides were not detected for the as-spun sample of the Ni-containing alloy. Previous works could not identify Ni on the surface either [72]. Only the peak corresponding Ni° metallic was found (852.9 eV). The contribution of NiO (854.3 eV) was encountered only in the sample heat-treated at 1000 °C.

As indicated above, the spectrum consists of peaks of the oxidized state of each element present in the composition and the elements in the metallic state, suggesting that we have an oxide layer in all cases. Given that a contribution of the metallic species could be detected, the metallic state peaks were assumed to come from the underlying alloy surface, and one can say that the XPS signal is composed of the passive film and the underlying alloy. Hence, since the maximum penetration depth is between 5 and 7 nm [73], one can say that the oxide layer has a thickness inferior to 7 nm. A compact, thin oxide layer can be associated with the high protectiveness of the passive film and, hence, good corrosion resistance. However, homogeneity is also an important parameter to consider [74].

Curve fitting was used to determine the oxide content.

The addition of metalloids was identified as beneficial for the corrosion resistance of Fe-Cr alloys [22]. The elements with high oxygen affinity, like Cr, Mo, and B, tend to concentrate on the surface when exposed to the air or corrosive solutions. The affinity of Mo with oxygen is way lower than Cr and Nb. For example, they will have preferential oxidation and be formed under Mo's outer layer. Many authors reported the excellent stability of Cr oxides of Fe-based alloys [75,76]

$$Cr \rightarrow Cr^{3+} + 3e^-, \tag{14}$$

$$Cr^{3+} + H_2O \rightarrow Cr(OH)_3 + 3H^+, \tag{15}$$

$$Cr(OH)_3 + 5OH^- \rightarrow CrO_4^{2-} + 4H_2O + 3e^-, \tag{16}$$

The presence of anions such as CrO_4^{2-} and MoO_4^{2-} are responsible for ion selectivity, hindering the penetration of aggressive chloride ions in the passive film [67]. However, borates were not found to be able to change the ion-selectivity of Cl^-, which indicates that the protection provided by B oxides is not as adequate as that offered by others, such as Cr and Nb oxides. Similar behavior was confirmed/observed by Virtanem [77] when studying passive film formation on Fe-Cr-(B, P)-C alloys. Molybdenium's role in combatting pitting corrosion is still in debate, even if many studies have been done in this field. Many studies point to Mo as responsible for passive film repair / re-passivation [72,78,79]. Some studies also point out Mo as accountable for protecting the passive film, preventing Cl- ions attack, and reducing pitting events. According to Figs. 7 and 8(c), Mo is found in the passive layer in the metallic state Mo and Mo^{4+} and Mo^{6+} states. Insoluble $FeMoO_4$ can be formed by the reaction between the Fe^{2+} and $MoO_2{}^4$, hindering pitting corrosion propagation.

Peak deconvolution allows the identification of oxidized species and further calculation of the concentration of each element on the surface through the integrated intensity area of each peak. For that, the sensitive factor associated with each element was considered. The values are shown in Table S2.

Fig. 9 shows the relative amounts (Area of the X oxide / Biggest Sum of the areas of all the oxides/hydroxides present in the layer in both alloys, assuming that the closest temperatures were the same: 570–640, 690–720, and 810–820) of each element in the oxidized state (OS) present in the passive film. Also, data from Table 1 (corrosion potentials and currents) are plotted in Fig. 9a and b to facilitate discussion further. We observe, for the Nb-containing alloy, a decrease of protective elements such as OS-Cr (25–19%), OS-Mo (Mo went from 10% to 2% when annealing the amorphous ribbons at 810 °C and was not even detected in the 1000 °C) and OS-Nb (going from representing 37% of film composition to only 10% when heat treated at 810 °C).

Moreover, the presence of OS-Nb was not detected at 1000 °C, when increasing the annealing temperature. It is well known that OS-Cr and OS-Mo oxides are denser than Fe-oxides, generally showing a porous structure. A similar behavior (OS-Nb) was observed by Yang [80] when analyzing Fe-based alloys as coatings in the amorphous state and after crystallization. However, Ni-containing alloy keeps a similar proportion of those elements for the as-spun sample until the second heat treatment explaining the weak difference in the polarization curve for those three samples. OS-Cr variation was more pronounced after the third cycle of annealing (820 °C), decreasing from 26% in the as-spun to 8%.

The thickness of the passive film is an important parameter, and XPS can be used as a reliable technique for pure metals. However, when it comes to multicomponent alloys, the determination can be a difficult task since oxidation is not homogeneous. Different calculation approaches can be found in the literature [27,28,81]. In the present study, for a comparative estimation of the oxide thickness, Eq. 17 was used.

$$d = \lambda \ln\left[1 + \frac{I_{M,ox}}{I_{M,met}}\right], \tag{17}$$

where d is the thickness of the oxide layer, λ is the inelastic mean free path of the oxide (values obtained from [82,83]) $I_{M,ox}/I_{M,met}$ represents

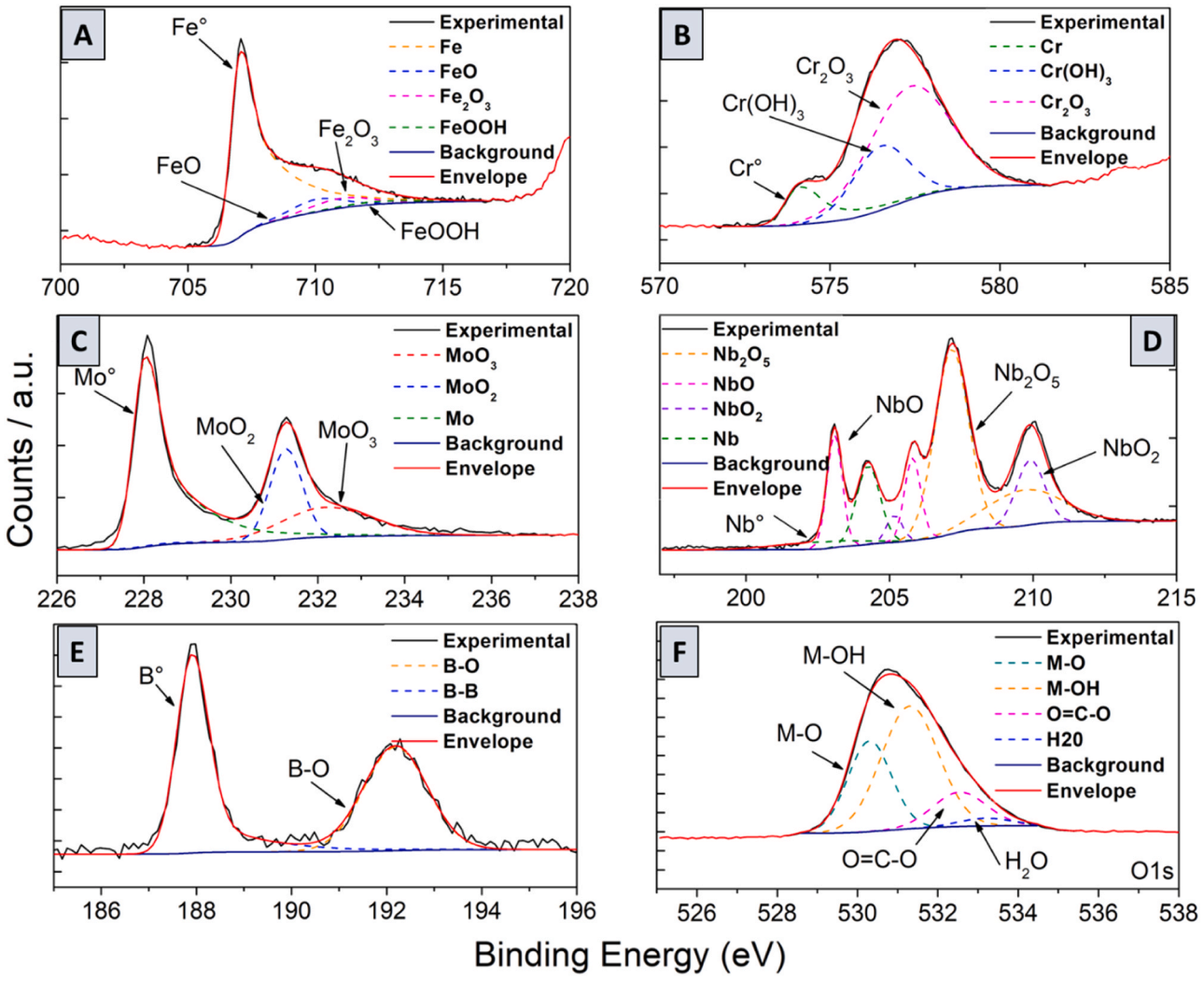

Fig. 7. XPS spectra for each element present in the passive film for the as-spun ribbon of the Nb-containing composition. The solid black line represents the experimental data, the red line represents the fitting, and the colored dotted lines indicate the different contributions of each element. Shirley's baseline (in dark blue) was applied. In (a) Fe2p; (b) Cr2p; (c) Mo3d; (d) Nb; (e) B; (f) O1s.

the ratio between the area of the oxide peak of the element M and the area of the element M, considering the sensitivity factor of each element (Table S2 – supplementary material). The thickness, t, was estimated based on the proportion of oxides present in the passive film (Fig. 9), to better represent the compositional complexity of the film apart from the B oxide, which showed the highest associated error.

The values obtained for the thickness of the passive layer for the samples of both alloys were less than 7 nm [73], typical of a thin and compact layer. Although higher, the values showed the same trend in the EIS results. For the Nb alloy, a value of 2.8 nm was found for the as-spun sample, which increased to 6.6 nm for the sample heat-treated at 640°C. The value of the sample treated at 720°C was smaller, reaching 4.8 nm. These results do not consider the contamination layer associated with C1s in the spectrum, resulting in higher obtained values.

The Ni-containing alloy showed the same trend, with the highest thickness value found for the sample treated at 570°C. The as-spun sample had a thickness of 4.9 nm. However, comparing the as-spun samples of the two studied alloys, the behavior was opposite to that presented by EIS, with the sample of the Ni-containing alloy showing a higher d value than the sample of the Nb-containing alloy. This behavior can be explained by various factors, including errors associated with estimating thickness via XPS, given that simplifications are made in the equation, and the proportion between the elements considered for the calculation also has a level of uncertainty. Furthermore, the value of the oxide permittivity ε was considered the same for all the samples to simplify the calculations, as in the case of complex passive layers containing various oxides, this value is difficult to determine precisely. Since the calculation of the thickness by EIS is sensitive to the value of ε, this is also a source of errors in the estimation.

Although these are only approximations, two aspects are worth mentioning: the values below 7 nm are typical of a thin, compact oxide layer such as a passivation layer. In addition, the values indicate that the ribbons did not undergo significant oxidation during the heat treatment process, i.e., the Ar atmosphere effectively protected the sample surface.

4. Discussion

This work successfully used a combination of potentiodynamic polarization curves, EIS, and XPS techniques to extract information on the behavior of two new Fe-based PHE alloys.

By analyzing the potentiodynamic curves, it is possible to observe two main behaviors. The first group comprises samples exhibiting a passive plateau, including samples in the amorphous state and those subjected to heat treatment in both alloys studied. The second category consists of samples heated at temperatures above 800 °C, which experienced generalized corrosion when exposed to an anodic potential.

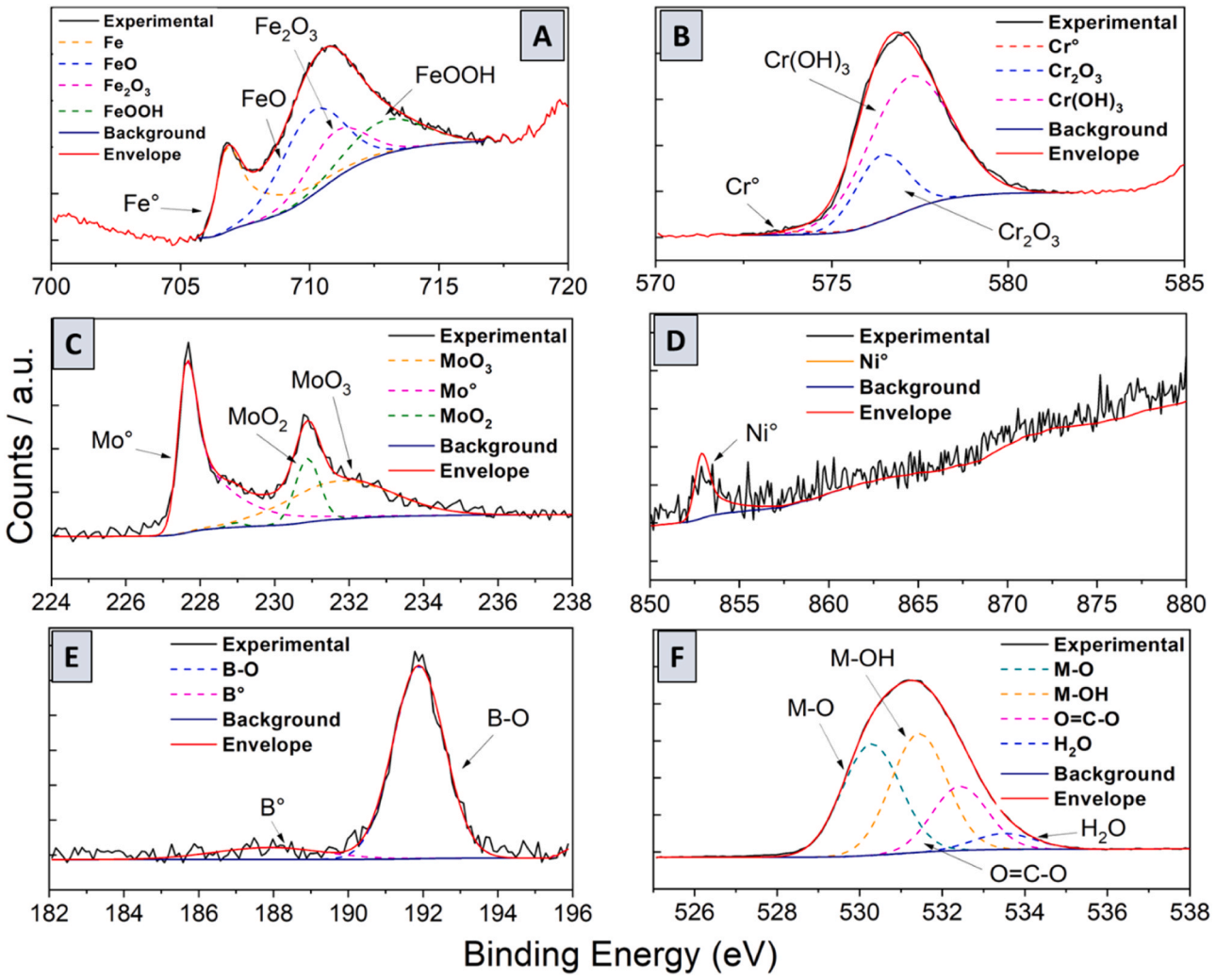

Fig. 8. XPS spectra for each element present in the passive film for the as-spun ribbon of the Ni-containing composition. The solid black line represents the experimental data, the red line represents the fitting, and the colored dotted lines indicate the different contributions of each element. Shirley's baseline (in dark blue) was applied. In (a) Fe2p; (b) Cr2p; (c) Mo3d; (d) Ni; (e) B; (f) O1s.

When we compare the two compositions, the Nb-containing alloy has an $i_{0.2V vs OCP}$ of about 10^{-8} A cm^{-2}, two decades less than the Ni-containing alloy (10^{-6} A cm^{-2}). The Nb-containing alloy shows an outstanding corrosion behavior compared to most of the alloys presented in the literature [14,15,45,50,80,84,85].

The Niobium oxide is often presented in the literature as a compact and resistant oxide and is responsible for changing the structure of the oxide layer, improving its protective properties[23]. Furthermore, the XPS analyses pointed out the presence of a layer rich in various oxides, including Nb oxides, for the Nb-containing alloy. At the same time, Ni was not identified in oxide form for the as-spun sample, which may be one of the explanations for the superior corrosion resistance of the alloy containing Nb.

The oxidation of multicomponent alloys is a competitive process. This process is evident in the XPS results presented in Fig. 8 and S7 for both alloys. As one may observe in these Figures, the amounts of the same oxides in both cases are very different depending on the presence of Nb or Ni (please also refer to Fig. 9). The explanation for this behavior can be extracted from the Ellingham [86] and Ellingham-Richardson [87,88], where one may observe that all the oxides detected by our XPS analyses on the surface are more stable than nickel oxide (NiO). Therefore, Ni did not form an oxide in the as-spun sample or in the early stages of heat treatment due to its low amount. NiO was only observed in the fully crystalline sample, likely because the other elements were less available once the precipitates had formed and also most probably used to stabilize the austenite phase as it happens in a standard Ni-alloyed stainless steel and also observed in the XRD pattern of Figure S1. Apparently, Ni remains in the matrix even at extremely high temperatures, up to 690 °C. Its oxidation is prevented by the formation of more stable oxides. At 820 °C, the austenite phase precipitates, and all available Ni is used up. At 1000 °C, Mo, Fe, and Cr are involved in the process of precipitates and the formation of the new bcc matrix allowing Ni oxides and hydroxides to be formed.

Also, Cr oxide is more stable than Ni oxide and Fe oxide. Nb oxide is more stable than any other oxide, and Mo oxide is more stable than Ni but less stable than Fe oxide [86–88]. Therefore, by observing the XPS results, one will notice that they present this trend precisely: There is a considerable amount of Cr oxide (there is no metallic Cr), a significant amount of Fe and Mo oxides, and a small amount of metallic Fe and Mo.

Furthermore, since metallic elements could be detected, it indicates that their electrons originate from the layer just beneath the oxide layer, corresponding to the metallic alloy. Considering the limit of electron penetration, it can be concluded that this is a thin layer. According to reference [89], the XPS beam has a penetration depth of only 5–7 nm. Therefore, it can be inferred that the film thickness is less than 7 nm, which supports the results obtained from the EIS analysis and XPS calculation.

As one may observe in Fig. 9, it is demonstrated that Ni has almost no

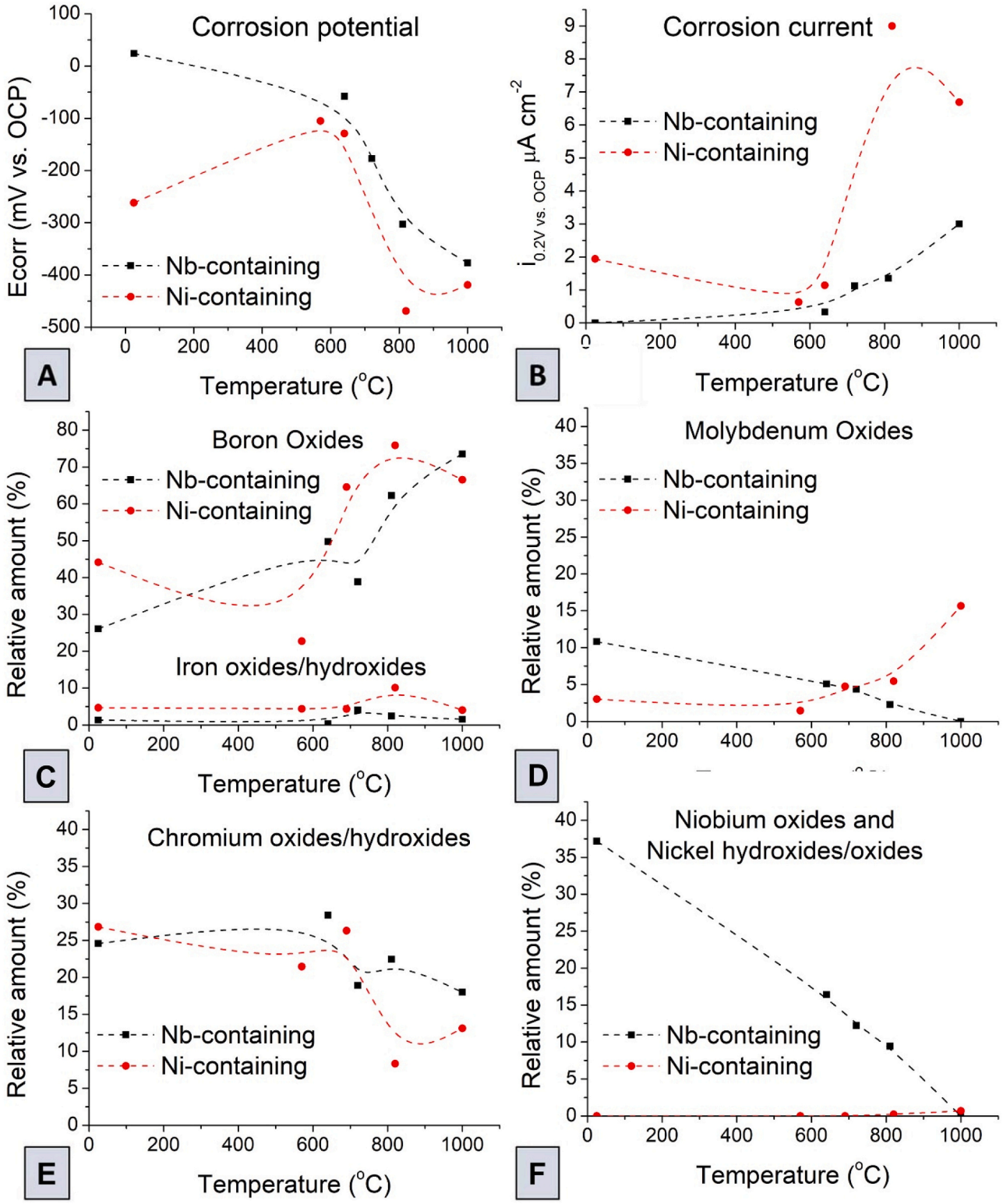

Fig. 9. Plots of corrosion data taken from Table 1, (a) potentials and (b) currents. Relative proportion of Fe, Cr, Mo, Nb, Ni, and B-compounds in the oxidized states on (a) FeCrMoNbB and (b) FeCrMoNiB alloy surface after 2 hours of immersion in a 35 g L^{-1} NaCl solution, natural pH of 5.5 and 25 °C, obtained from the analysis of the XPS spectra.

influence in the Ni-containing alloy, but Mo does, as the amount of OS-B drops with the increase in OS-Mo. In this case, it is very clear that OS-Cr is the main one in both alloys because OS- B and OS-Fe behave with the inverse of OS- Cr. Still, OS-Nb and OS-Mo have a significant impact on the alloy because the amount of OS-B increases with their decrease. On the other hand, OS-Ni has almost no influence on Ni-containing alloy, unlike OS-Mo, which, along with OS-Cr, shows a strong influence. An increase in OS-Mo and OS-Cr decreases the amount of OS-B and OS-Fe.

Indeed, evaluating the passivation, as one may observe in Fig. 9, there is a synergism between Cr, Nb, and Mo in the passive film of the

Nb-containing alloy and Cr and Mo in the passive film of the Ni-containing one, directly impacting the overall corrosion potential (Ecorr) behavior. In other words, it is evident that Ecorr decreases with the decrease of Cr, Nb, and Mo in the film of the Nb-containing alloy and Cr and Mo in the Ni-containing one. Also, the levels of Ecorr in the film of the Nb-containing alloy are always higher than for the Ni-containing one due to, in addition to the effect of OS-Mo and OS-Nb, the higher contents of OS-Cr in all temperature conditions. Furthermore, the variations around the average value (dash line) are directly related to variations in OS-Cr, not only for the Nb-containing alloy but also for the Ni-containing one.

Considering the Ni-containing alloy, observing the strong influence of OS-Cr is interesting. As almost no other OS-Element contributes to the passive film up to about 800 °C other than OS-Cr, such passive film may be a reference for analyzing its influence on both alloys' surfaces. From that temperature range results, it is possible to observe that an increase of only 5% of OS-Cr leads to an increase of about 100 mV in Ecorr. This effect is almost directly proportional because, with a decrease of about 40% in OS-Cr, the potential is decreased by about 350 mV. The effect of OS-Nb and OS-Mo in the passive film of the Nb-containing alloy can be inferred by the vast difference in Ecorr between both passive films of both alloys in almost the same temperature range. The OS-Mo effect on the surface film of the Ni-containing alloy may be observed at the temperature of 1000 °C, where the OS-Cr hugely dropped, but Ecorr increased with the increase of OS-Mo.

Regarding corrosion current, the behaviors are very similar to the ones for the OS-B and OS-Fe described above, and the explanation related to the film formation and passivation may be the same. However, more notable is the influence of the synergetic effect of OS-Cr, OS-Mo, and OS-Nb in the passive film of the Nb-containing alloy on the corrosion currents behaviors. Such currents are always smaller than the ones for the Ni-containing alloy, probably because of the highest amounts of OS-Cr in all temperature conditions, but the whole behavior is almost coincident with the inverse of their decreased amount in the surface film. The same may be applied to OS-Cr and OS-Mo in the passive film of the Ni-containing alloy because, as one may observe in the Figure, the currents drop with their increasing amounts.

The fitting with SIMAD allowed estimating the resistivity values ρ_0 and ρ_δ. By comparing the as-spun samples of both compositions, the Nb-containing alloy presents a higher value of ρ_0 (metal/oxide interface) compared to the Ni-containing alloy, corroborating the general idea that the Nb-containing alloy gives better corrosion resistance. By comparing the as-spun and heat-treated samples in the case of both alloys, the resistivity profile proved to be quite consistent with the behavior observed through the potentiodynamic curves, with a decrease in the values of ρ_0 and ρ_δ for the Nb-containing alloy with increasing of temperature. For the Ni-containing alloy, after heat treatment at 690°C, the resistivity ρ_0 value is similar. However, the ρ_δ was superior for the heat-treated sample, consistent with the behavior observed by the potentiodynamic curves and was similar, but slightly better, for the heat-treated sample.

After crystallization, a significant decrease in the percentage of protective oxides in the passive layer is observed, especially Nb oxides, which represent about 35% for the as-spun sample, and were not detected for the 1000 °C heat-treated sample. This behavior is associated with forming precipitates rich in these protective elements such as Nb, which are no longer available to create the passive film. This decrease in protective elements, associated with increased surface heterogeneity and the formation of defects resulting from the crystallization process, reflects a degradation of corrosion properties. observed by the potentiodynamic curves. On the other hand, this reduction is not observed in the case of the alloy containing Ni, which presents similar $i_{0.2VvsOCP}$ and E_{corr} values at temperatures below 700 °C. A specific model has been developed to describe the interface for these cases.

It is worth emphasizing that the alloys presented in this study do not exhibit pitting corrosion, contrary to most in the literature [51,90–92]. The impedance analysis for the samples of both compositions resulted in capacitance values and thickness typical of a passive protective layer. The samples presenting a CPE behavior were extracted for the first time in the literature for PHEA fit using power law and resistivity values of about 10^{13} Ω cm^2 for as-pun alloy samples containing Nb. This value decreased by one decade compared to the same alloy sample containing Ni. For the cases where samples showed a passive plateau, the combination of MM, SIMAD, cole-cole, and XPS results allowed the extraction of valuable information about the passive film.

Fig. 10 shows a schematic representation of the interface metal/oxide layer/electrolyte for the proposed samples analyzed in this work. The Power law defines the presence of a high film resistance associated with a high film protection capacity.

In the case of the metal in contact with the electrolyte, the metal can dissolve into the electrolyte. The oxide layer will depend on the oxide structure and composition and is independent of the reactions at the interface metal-electrolyte. The velocity of the charge transfer depends on the kind of reaction, temperature, potential, and concentration of reaction products.

5. Conclusions

After analyzing the results and discussing them, certain conclusions can be made.

- The behavior of multicomponent alloys proved to be quite complex. Despite exhibiting relatively similar polarization curves, using the impedance technique and multiple tools such as Cole-Cole and MM, combined with XPS analysis, allowed the extraction of resistivity at the metal/oxide interface, thickness, and capacitance, enabling the calculation of resistivity ρ_δ and the consequent plotting of the resistivity profile.
- The resistivity profile was plotted for two samples of each composition, namely the as-spun and those heat-treated at approximately 700°C, and demonstrated consistency with the behavior observed in the potentiodynamic curves. Typical insulator-like resistivity values were found at the metal/oxide interface for the samples, even after annealing at temperatures close to 700 °C.
- A decrease of up to about 50% in the amorphous phase did not impair the corrosion properties of the Ni-containing alloy samples. For both compositions, heat treatment above 800 °C completely degrades the corrosion properties of the alloy; generalized corrosion is observed.
- The analysis of XPS shows that the presence of Nb oxide significantly influences the corrosion behavior. The decrease in the percentage of this oxide and protective oxides such as Cr and Mo in the passive film was associated with a degradation of corrosion properties.

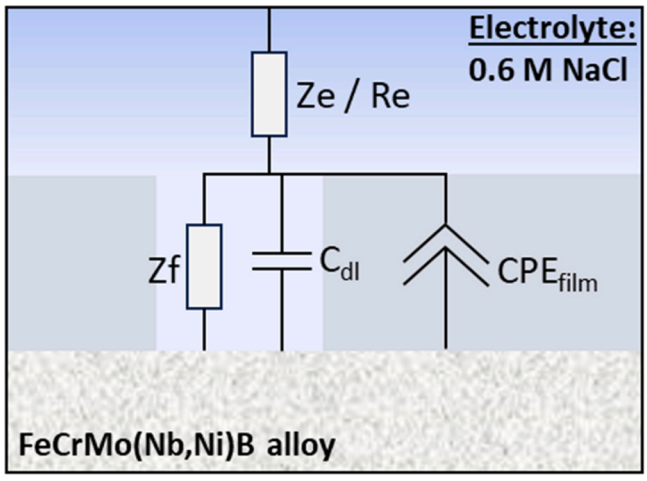

Fig. 10. – Schematic representation of the interface alloy/oxide film/electrolyte for an oxide layer partially covering the surface.

- Limitations concerning the techniques were also emphasized. Notably, the Cole-Cole plot's sensitivity to accurately estimate the value of Re was highlighted, along with potential errors associated with using approximate values for the material's permittivity. Additionally, errors in calculating thickness via XPS were attributed to the simplification of the equations utilized and the inability to access the oxide structure in greater detail.

CRediT authorship contribution statement

Champion Yannick: Writing – review & editing, Validation, Methodology, Conceptualization. **Roche Virginie:** Writing – review & editing, Visualization, Validation, Supervision, Resources, Project administration, Methodology, Conceptualization. **Mantel Marc:** Writing – review & editing, Visualization, Validation, Supervision, Resources, Methodology, Conceptualization. **Weverson C. Batalha:** Writing – review & editing, Writing – original draft, Validation, Methodology, Investigation, Formal analysis, Conceptualization. **Jorge Junior Alberto M.:** Writing – review & editing, Visualization, Validation, Supervision, Resources, Methodology, Conceptualization.

Declaration of Competing Interest

The authors declare that they have no known competing financial interests or personal relationships that could have appeared to influence the work reported in this paper.

Data Availability

Data will be made available on request.

Acknowledgments

The French National Research Agency supports this work in the "Investissements d'avenir" program (ANR-15-IDEX-02) framework. W.C. B. thanks the L'Initiative d'excellence (IDEX) Université Grenoble Alpes under the project Initiatives de Recherche Stratégiques (IRS) for his salary. The authors are also grateful to Le Consortium des Moyens Technologiques Communs (CMTC – Grenoble-INP-France) and The Centre of Excellence of Multifunctional Architectured Materials (CEMAM) for the use of its facilities. A.M.J.J acknowledges the National Council for Scientific and Technological Development - CNPq (Brazil) under grant #306622/2021-1 and the São Paulo Research Foundation - FAPESP (Brazil) under grant FAPESP # 2021/06546-1.

Appendix A. Supporting information

Supplementary data associated with this article can be found in the online version at doi:10.1016/j.corsci.2024.111905.

References

[1] M.P. Ryan, D.E. Williams, R.J. Chater, B.M. Hutton, D.S. McPhail, Why stainless steel corrodes, Nature 415 (2002) 770–774, https://doi.org/10.1038/415770a.
[2] J. Soyama, G. Zepon, T.P. Lopes, L. Beraldo, C.S. Kiminami, W.J. Botta, C. Bolfarini, Microstructure formation and abrasive wear resistance of a boron-modified superduplex stainless steel produced by spray forming, J. Mater. Res. 31 (2016) 2987–2993, https://doi.org/10.1557/jmr.2016.323.
[3] G.Y. Koga, C. Bolfarini, C.S. Kiminami, A.M. Jorge, W.J. Botta, An Overview of Thermally Sprayed Fe-Cr-Nb-B Metallic Glass Coatings: From the Alloy Development to the Coating's Performance Against Corrosion and Wear, 2022. ⟨https://doi.org/10.1007/s11666-022-01371-7⟩.
[4] R. Badyka, S. Saillet, C. Domain, C. Pareige, Effect of annealing treatment at 550 °C on ferrite of thermally aged cast austenitic stainless steels and ageing kinetics of reverted cast austenitic stainless steels, J. Nucl. Mater. 542 (2020) 152530, https://doi.org/10.1016/j.jnucmat.2020.152530.
[5] G.Y. Koga, T. Ferreira, Y. Guo, D.D. Coimbrão, A.M. Jorge, C.S. Kiminami, C. Bolfarini, W.J. Botta, Challenges in optimizing the resistance to corrosion and wear of amorphous Fe-Cr-Nb-B alloy containing crystalline phases, J. Non Cryst. Solids 555 (2021), https://doi.org/10.1016/j.jnoncrysol.2020.120537.
[6] S. Pang, T. Zhang, K. Asami, A. Inoue, Synthesis of Fe–Cr–Mo–C–B–P bulk metallic glasses with high corrosion resistance, Acta Mater. 50 (2002) 489–497, https://doi.org/10.1016/S1359-6454(01)00366-4.
[7] M. Iqbal, J.I. Akhter, H.F. Zhang, Z.Q. Hu, Synthesis and characterization of bulk amorphous steels, J. Non Cryst. Solids 354 (2008) 3284–3290, https://doi.org/10.1016/j.jnoncrysol.2008.02.009.
[8] H. Zhang, Z.C. Yan, Q. Chen, Y. Feng, Z.G. Qi, H.Z. Liu, X.Y. Li, W.M. Wang, Hardness, magnetism and passivation of Fe-Si-B-Nb glasses, J. Non Cryst. Solids 564 (2021), https://doi.org/10.1016/j.jnoncrysol.2021.120830.
[9] L. Liu, C. Zhang, Fe-based amorphous coatings: structures and properties, Thin Solid Films 561 (2014) 70–86, https://doi.org/10.1016/j.tsf.2013.08.029.
[10] Z.B. Zheng, Y.G. Zheng, W.H. Sun, J.Q. Wang, Erosion-corrosion of HVOF-sprayed Fe-based amorphous metallic coating under impingement by a sand-containing NaCl solution, Corros. Sci. 76 (2013) 337–347, https://doi.org/10.1016/j.corsci.2013.07.006.
[11] M.A. Maruf, S.M.M. Rizvi, M. Noor-A-Alam, D. Shin, W. Haider, I. Shabib, Corrosion resistance and thermal stability of sputtered Fe44Al34Ti7N15 and Al61Ti11N28 thin films for prospective application in oil and gas industry, Prog. Nat. Sci. Mater. Int. 31 (2021) 688–697, https://doi.org/10.1016/j.pnsc.2021.09.005.
[12] X. Ji, J. Zhao, X. Zhang, M. Zhou, Erosion-corrosion behavior of Zr-based bulk metallic glass in saline-sand slurry, Tribol. Int. 60 (2013) 19–24, https://doi.org/10.1016/j.triboint.2012.10.010.
[13] K. Kishitake, H. Era, F. Otsubo, Thermal-sprayed Fe-10CM^{3}P–^{7}C amorphous coatings possessing excellent corrosion resistance, J. Therm. Spray. Technol. 5 (1996) 476–482, https://doi.org/10.1007/BF02645279.
[14] M.J. Duarte, J. Klemm, S.O. Klemm, K.J.J. Mayrhofer, M. Stratmann, S. Borodin, a H. Romero, M. Madinehei, D. Crespo, J. Serrano, S.S. a Gerstl, P.P. Choi, D. Raabe, F.U. Renner, Element-Resolved Corrosion, Science 372 (80) (2013) 372–377.
[15] M.J. Duarte, A. Kostka, J.A. Jimenez, P. Choi, J. Klemm, D. Crespo, D. Raabe, F. U. Renner, Crystallization, phase evolution and corrosion of Fe-based metallic glasses: An atomic-scale structural and chemical characterization study, Acta Mater. 71 (2014) 20–30, https://doi.org/10.1016/j.actamat.2014.02.027.
[16] W.C. Batalha, V. Roche, Y. Champion, M. Mantel, M. Verdier, V. Martin, C. S. Kiminami, A.M. Jorge Junior, Newly-developed pseudo-high entropy amorphous alloys: Structure/microstructure evolution, mechanical and corrosion properties, J. Non Cryst. Solids 613 (2023) 122369, https://doi.org/10.1016/j.jnoncrysol.2023.122369.
[17] M.-H. Tsai, J.-W. Yeh, High-entropy alloys: a critical review, Mater. Res. Lett. 2 (2014) 107–123, https://doi.org/10.1080/21663831.2014.912690.
[18] A. Inoue, Z. Wang, D.V. Louzguine-Luzgin, Y. Han, F.L. Kong, E. Shalaan, F. Al-Marzouki, Effect of high-order multicomponent on formation and properties of Zr-based bulk glassy alloys, J. Alloy. Compd. 638 (2015) 197–203, https://doi.org/10.1016/j.jallcom.2015.03.078.
[19] A. Hirata, Y. Hirotsu, K. Amiya, A. Inoue, Crystallization process and glass stability of an Fe48Cr15Mo14C15B6Tm2 bulk metallic glass, Phys. Rev. B. 78 (2008) 144205, https://doi.org/10.1103/PhysRevB.78.144205.
[20] X. Li, A. Makino, K. Yubuta, H. Kato, A. Inoue, Mechanical properties of soft magnetic (Fe0.76Si0.096B0.084P0.06)100−xCux (x=0 and 0.1) Bulk Glassy Alloys, Mater. Trans. 50 (2009) 1286–1289, https://doi.org/10.2320/matertrans.ME200833.
[21] H. Zhang, Z.C. Yan, K.C. Shen, Q. Chen, L.C. Zhang, X.Y. Li, W.M. Wang, Potentiodynamic and potentiostatic investigation on the passivation of Fe based glassy alloys in alkaline solution, J. Alloy. Compd. 857 (2021), https://doi.org/10.1016/j.jallcom.2020.157573.
[22] M. Naka, K. Hashimoto, T. Masumoto, Effect of metalloidal elements on corrosion resistance of amorphous iron-chromium alloys, J. Non Cryst. Solids 28 (1978) 403–413, https://doi.org/10.1016/0022-3093(78)90090-X.
[23] H. Zhang, Z.C. Yan, Q. Chen, Y. Feng, Z.G. Qi, H.Z. Liu, X.Y. Li, W.M. Wang, Hardness, magnetism and passivation of Fe-Si-B-Nb glasses, J. Non Cryst. Solids 564 (2021) 120830, https://doi.org/10.1016/j.jnoncrysol.2021.120830.
[24] K.L. Cwalina, H.M. Ha, N. Ott, P. Reinke, N. Birbilis, J.R. Scully, In Operando Analysis of Passive Film Growth on Ni-Cr and Ni-Cr-Mo Alloys in Chloride Solutions, J. Electrochem. Soc. 166 (2019) C3241–C3253, https://doi.org/10.1149/2.0261911jes.
[25] T.J. Mesquita, E. Chauveau, M. Mantel, R.P. Nogueira, A XPS study of the Mo effect on passivation behaviors for highly controlled stainless steels in neutral and alkaline conditions, Appl. Surf. Sci. 270 (2013) 90–97, https://doi.org/10.1016/j.apsusc.2012.12.118.
[26] C. Man, C. Dong, D. Kong, L. Wang, X. Li, Beneficial effect of reversed austenite on the intergranular corrosion resistance of martensitic stainless steel, Corros. Sci. 151 (2019) 108–121, https://doi.org/10.1016/j.corsci.2019.02.020.
[27] B. Elsener, A. Rossi, XPS investigation of passive films on amorphous FeCr alloys, Electrochim. Acta 37 (1992) 2269–2276, https://doi.org/10.1016/0013-4686(92)85122-2.
[28] C.O.A. Olsson, D. Landolt, Atmospheric oxidation of a Nb-Zr alloy studied with XPS, Corros. Sci. 46 (2004) 213–224, https://doi.org/10.1016/S0010-938X(03)00139-2.
[29] A. Barroux, T. Duguet, N. Ducommun, E. Nivet, J. Delgado, L. Laffont, C. Blanc, Combined XPS / TEM study of the chemical composition and structure of the passive film formed on additive manufactured 17-4PH stainless steel, Surf. Interfaces 22 (2021), https://doi.org/10.1016/j.surfin.2020.100874.
[30] B. Tribollet, V. Vivier, M.E. Orazem, EIS technique in passivity studies: Determination of the dielectric properties of passive films, Elsevier Inc, 2018, https://doi.org/10.1016/B978-0-12-409547-2.13817-X.

[31] R.I. Revilla, B. Wouters, F. Andreatta, A. Lanzutti, L. Fedrizzi, I. De Graeve, EIS comparative study and critical Equivalent Electrical Circuit (EEC) analysis of the native oxide layer of additive manufactured and wrought 316L stainless steel, Corros. Sci. 167 (2020) 108480, https://doi.org/10.1016/j.corsci.2020.108480.

[32] Y.M. Chen, A.S. Nguyen, M.E. Orazem, B. Tribollet, N. Pébère, M. Musiani, V. Vivier, Identification of Resistivity Distributions in Dielectric Layers by Measurement Model Analysis of Impedance Spectroscopy, Electrochim. Acta 219 (2016) 312–320, https://doi.org/10.1016/j.electacta.2016.09.136.

[33] Y.-M. Chen, N.G. Rudawski, E. Lambers, M.E. Orazem, application of impedance spectroscopy and surface analysis to obtain oxide film thickness, J. Electrochem. Soc. 164 (2017) C563–C573, https://doi.org/10.1149/2.1061709jes.

[34] M. Diaz-Ramos, V. Roche, R. Song, H. Fan, C. Bureau, J.C. Lepretre, Electrochemical Impedance Spectroscopy (EIS) of parylene coated magnesium stents in organic solvent to study early corrosion control, Corros. Sci. 213 (2023) 110932, https://doi.org/10.1016/j.corsci.2022.110932.

[35] M.E.O.W. Watson, EIS: measurement model program, ECSarXiv (2020), https://doi.org/10.1149/osf.io/kze9x.

[36] H. Liao, W. Watson, A. Dizon, B. Tribollet, V. Vivier, M.E. Orazem, Physical properties obtained from measurement model analysis of impedance measurements, Electrochim. Acta 354 (2020), https://doi.org/10.1016/j.electacta.2020.136747.

[37] T. Jänsch, J. Wallauer, B. Roling, Influence of electrode roughness on double layer formation in ionic liquids, J. Phys. Chem. C. 119 (2015) 4620–4626, https://doi.org/10.1021/jp512617j.

[38] M. Benoit, C. Bataillon, B. Gwinner, F. Miserque, M.E. Orazem, C.M. Sánchez-Sánchez, B. Tribollet, V. Vivier, Comparison of different methods for measuring the passive film thickness on metals, Electrochim. Acta 201 (2016) 340–347, https://doi.org/10.1016/j.electacta.2015.12.173.

[39] D. Briggs, Handbook of X-ray Photoelectron Spectroscopy C. D. Wanger, W. M. Riggs, L. E. Davis, J. F. Moulder and G. E.Muilenberg Perkin-Elmer Corp., Physical Electronics Division, Eden Prairie, Minnesota, USA, 1979. 190 pp. $195, 1981. ⟨https://doi.org/10.1002/sia.740030412⟩.

[40] D.D. Coimbrão, G. Zepon, G.Y. Koga, D.A. Godoy Pérez, F.H. Paes de Almeida, V. Roche, J.C. Lepretre, A.M. Jorge, C.S. Kiminami, C. Bolfarini, A. Inoue, W. J. Botta, Corrosion properties of amorphous, partially, and fully crystallized Fe68Cr8Mo4Nb4B16 alloy, J. Alloy. Compd. 826 (2020), https://doi.org/10.1016/j.jallcom.2020.154123.

[41] Y. Wang, M.Y. Li, F. Zhu, W.T. Dong, X.Y. Zhang, L.L. Sun, Pitting corrosion mechanism of Cl−- and S2−-induced by oxide inclusions in Fe-based amorphous metallic coatings, Surf. Coat. Technol. 385 (2020), https://doi.org/10.1016/j.surfcoat.2020.125449.

[42] S. Liu, Y. Zhu, X. Lai, X. Zheng, R. Jia, X. Yuan, Influence of different heat treatment temperatures on the microstructure, corrosion, and mechanical properties behavior of fe-based amorphous/nanocrystalline coatings, Coatings 9 (2019), https://doi.org/10.3390/coatings9120858.

[43] A.A. Khan, A.A. Razin, D.S.S. Ahammed, M.S. Kaiser, Comparison of electrochemical corrosion performance of eutectic Al-Si automotive alloy in deep seawater and 3.5% NaCl solution, Mater. Today Proc. 82 (2023) 241–247, https://doi.org/10.1016/j.matpr.2023.01.179.

[44] M.J.F. Marques, A. Benedetti, F. Castelli, M. Delucchi, M. Faimali, S. Delsante, F. Valenza, F. Garaventa, G. Pavanello, R. Basseguy, Influence of natural seawater variables on the corrosion behaviour of aluminium-magnesium alloy, Bioelectrochemistry 149 (2023) 108321, https://doi.org/10.1016/j.bioelechem.2022.108321.

[45] G.Y. Koga, R.P. Nogueira, V. Roche, A.R. Yavari, A.K. Melle, J. Gallego, C. Bolfarini, C.S. Kiminami, W.J. Botta, Corrosion properties of Fe-Cr-Nb-B amorphous alloys and coatings, Surf. Coat. Technol. 254 (2014) 238–243, https://doi.org/10.1016/j.surfcoat.2014.06.022.

[46] D.D. Coimbrão, G. Zepon, G.Y. Koga, D.A.P. Godoy, F.H.P. De Almeida, V. Roche, J. Lepretre, A.M.J. Jr, C.S. Kiminami, C. Bolfarini, A. Inoue, Corrosion properties of amorphous, partially, and fully crystallized Fe68Cr8Mo4Nb4B16 alloy 826 (2020).

[47] G.Y. Koga, T. Ferreira, Y. Guo, A.M. Jorge, C.S. Kiminami, C. Bolfarini, W.J. Botta, Challenges in optimizing the resistance to corrosion and wear of amorphous Fe-Cr-Nb-B alloy containing crystalline phases, (n.d.).

[48] C.A.C. Souza, M.F. De Oliveira, J.E. May, W.J. Botta F, N.A. Mariano, S.E. Kuri, C. S. Kiminami, Corrosion resistance of amorphous and nanocrystalline Fe-M-B (M=Zr, Nb) alloys, J. Non Cryst. Solids 273 (2000) 282–288, https://doi.org/10.1016/S0022-3093(00)00174-5.

[49] K. Hashimoto, What we have learned from studies on chemical properties of amorphous alloys? Appl. Surf. Sci. 257 (2011) 8141–8150, https://doi.org/10.1016/j.apsusc.2010.12.142.

[50] A. Obeydavi, A. Shafyei, A. Rezaeian, P. Kameli, J.W. Lee, Microstructure, mechanical properties and corrosion performance of Fe44Cr15Mo14Co7C10B5Si5 thin film metallic glass deposited by DC magnetron sputtering, J. Non Cryst. Solids 527 (2020), https://doi.org/10.1016/j.jnoncrysol.2019.119718.

[51] C.S. Kiminami, C.A.C. Souza, L.F. Bonavina, L.R.P. De Andrade Lima, S. Suriñach, M.D. Baró, C. Bolfarini, W.J. Botta, Partial crystallization and corrosion resistance of amorphous Fe-Cr-M-B (M = Mo, Nb) alloys, J. Non Cryst. Solids 356 (2010) 2651–2657, https://doi.org/10.1016/j.jnoncrysol.2010.04.051.

[52] O. Gharbi, A. Dizon, M.E. Orazem, M.T.T. Tran, B. Tribollet, V. Vivier, From frequency dispersion to ohmic impedance: a new insight on the high-frequency impedance analysis of electrochemical systems, Electrochim. Acta 320 (2019) 134609, https://doi.org/10.1016/j.electacta.2019.134609.

[53] C. Blanc, M.E. Orazem, N. Pébre, B. Tribollet, V. Vivier, S. Wu, The origin of the complex character of the Ohmic impedance, Electrochim. Acta 55 (2010) 6313–6321, https://doi.org/10.1016/j.electacta.2010.04.036.

[54] M.E. Orazem, J.E. Soc, M.E. Orazem, N. Pébère, B. Tribollet, Enhanced Graphical Representation of Electrochemical Impedance Data Enhanced Graphical Representation of Electrochemical, (2006). ⟨https://doi.org/10.1149/1.2168377⟩.

[55] P. Córdoba-Torres, N.T.C. Oliveira, C. Bolfarini, V. Roche, R.P. Nogueira, Electrochemical impedance analysis of TiO2 nanotube porous layers based on an alternative representation of impedance data, J. Electroanal. Chem. 737 (2015) 54–64, https://doi.org/10.1016/j.jelechem.2014.06.034.

[56] A. González-Cortés, Electrochemical Impedance Spectroscopy. Agric. Food Electroanal., John Wiley & Sons, Ltd, Chichester, UK, 2015, pp. 381–419, https://doi.org/10.1002/9781118684030.ch14.

[57] B. Hirschorn, M.E. Orazem, B. Tribollet, V. Vivier, I. Frateur, M. Musiani, Constant-phase-element behavior caused by resistivity distributions in films, J. Electrochem. Soc. 157 (2010) C458, https://doi.org/10.1149/1.3499565.

[58] M.E. Orazem, I. Frateur, B. Tribollet, V. Vivier, S. Marcelin, N. Pébère, A.L. Bunge, E.A. White, D.P. Riemer, M. Musiani, dielectric properties of materials showing constant-phase-element (CPE) Impedance Response, J. Electrochem. Soc. 160 (2013) C215–C225, https://doi.org/10.1149/2.033306jes.

[59] Y.J. Sun, R. Yang, L. Xie, Y.B. Li, S.L. Wang, H.X. Li, W.R. Wang, J.S. Zhang, Interfacial bonding and corrosion behaviors of HVOF-sprayed Fe-based amorphous coating on 8090 Al-Li alloy, Surf. Coat. Technol. 436 (2022), https://doi.org/10.1016/j.surfcoat.2022.128316.

[60] L. Freire, X.R. Nóvoa, M.F. Montemor, M.J. Carmezim, Study of passive films formed on mild steel in alkaline media by the application of anodic potentials, Mater. Chem. Phys. 114 (2009) 962–972, https://doi.org/10.1016/j.matchemphys.2008.11.012.

[61] P. Agarwal, M.E. Orazem, L.H. Garcia-Rubio, Measurement models for electrochemical impedance spectroscopy: i. demonstration of applicability, J. Electrochem. Soc. 139 (1992) 1917–1927, https://doi.org/10.1149/1.2069522.

[62] J. Tang, L. Yu, J. Qiao, Y. Wang, H. Wang, M. Duan, M. Chamas, Effect of atomic mobility on the electrochemical properties of a Zr58Nb3Cu16Ni13Al10 bulk metallic glass, Electrochim. Acta 267 (2018) 222–233, https://doi.org/10.1016/j.electacta.2018.02.071.

[63] D. Liang, J.C. Tseng, X. Liu, Y. Cai, G. Xu, J. Shen, Investigation of the structural heterogeneity and corrosion performance of the annealed fe-based metallic glasses, Mater. (Basel) 14 (2021) 1–14, https://doi.org/10.3390/ma14040929.

[64] B. Hirschorn, M.E. Orazem, B. Tribollet, V. Vivier, I. Frateur, M. Musiani, Constant-phase-element behavior caused by resistivity distributions in films, J. Electrochem. Soc. 157 (2010) C452, https://doi.org/10.1149/1.3499564.

[65] S. Marcelin, Z. Zhang, B. Ter-Ovanessian, B. Normand, relationship between the resistivity profiles obtained from the power law model and the physico-chemical properties of passive films, J. Electrochem. Soc. 168 (2021) 021503, https://doi.org/10.1149/1945-7111/abde84.

[66] Č. Donik, A. Kocijan, J.T. Grant, M. Jenko, A. Drenik, B. Pihlar, XPS study of duplex stainless steel oxidized by oxygen atoms, Corros. Sci. 51 (2009) 827–832, https://doi.org/10.1016/j.corsci.2009.01.021.

[67] S. Virtanen, H. Böhni, Passivity, breakdown and repassivation of glassy Fe□Cr□P alloys, Corros. Sci. 31 (1990) 333–342, https://doi.org/10.1016/0010-938X(90)90128-R.

[68] J. Li, L. Yang, H. Ma, K. Jiang, C. Chang, J. Wang, Z. Song, X. Wang, R. Li, Improved corrosion resistance of novel Fe-based amorphous alloys, JMADE 95 (2016) 225–230, https://doi.org/10.1016/j.matdes.2016.01.100.

[69] T. Hanawa, S. Hiromoto, K. Asami, Characterization of the surface oxide film of a Co-Cr-Mo alloy after being located in quasi-biological environments using XPS, Appl. Surf. Sci. 183 (2001) 68–75, https://doi.org/10.1016/S0169-4332(01)00551-7.

[70] M.J.M. Pires, W.A.A. Macedo, L.P. Cavalcanti, A.M.G. Carvalho, characterization of Fe-Nb sputtered thin films, J. Phys. Chem. Solids 86 (2015) 36–41, https://doi.org/10.1016/j.jpcs.2015.06.012.

[71] R. Jain, D. Bhandari, A. Dhawan, S.K. Sharma, Characterization of native oxide film on amorphous Co66Si16B12Fe4Mo2 by X-ray photoelectron spectroscopy, J. Alloy. Compd. 490 (2010) 613–617, https://doi.org/10.1016/j.jallcom.2009.10.119.

[72] B. Lynch, F. Wiame, V. Maurice, P. Marcus, XPS study of oxide nucleation and growth mechanisms on a model FeCrNiMo stainless steel surface, Appl. Surf. Sci. 575 (2022) 151681, https://doi.org/10.1016/j.apsusc.2021.151681.

[73] R.W. Welker, Chapter 4 - Size Analysis and Identification of Particles, in: Rajiv Kohli, K.L. Mittal (Eds.), Dev. Surf. Contam. Clean., Elsevier,, 2012, pp. 179–213, https://doi.org/10.1016/B978-1-4377-7883-0.00004-3.

[74] Y. Waseda, K.T. Aust, Corrosion behaviour of metallic glasses, J. Mater. Sci. 16 (1981) 2337–2359, https://doi.org/10.1007/BF01113569.

[75] S. Li, Q. Wei, Q. Li, B. Jiang, Y. Chen, Y. Sun, Development of Fe-based bulk metallic glasses as potential biomaterials, Mater. Sci. Eng. C. 52 (2015) 235–241, https://doi.org/10.1016/j.msec.2015.03.041.

[76] Y.B. Wang, H.F. Li, Y.F. Zheng, M. Li, Corrosion performances in simulated body fluids and cytotoxicity evaluation of Fe-based bulk metallic glasses, Mater. Sci. Eng. C. 32 (2012) 599–606, https://doi.org/10.1016/j.msec.2011.12.018.

[77] S. Virtanen, E.M. Moser, H. Böhni, XPS studies on passive films on amorphous Fe-Cr-(B,P)-C alloys, Corros. Sci. 36 (1994) 373–384, https://doi.org/10.1016/0010-938X(94)90163-5.

[78] J.B. Lee, Effects of alloying elements, Cr, Mo and N on repassivation characteristics of stainless steels using the abrading electrode technique, Mater. Chem. Phys. 99 (2006) 224–234, https://doi.org/10.1016/j.matchemphys.2005.10.016.

[79] A. Elbiache, P. Marcus, The role of molybdenum in the dissolution and the passivation of stainless steels with adsorbed sulphur, Corros. Sci. 33 (1992) 261–269, https://doi.org/10.1016/0010-938X(92)90150-2.

[80] Y. Yang, C. Zhang, Y. Peng, Y. Yu, L. Liu, Effects of crystallization on the corrosion resistance of Fe-based amorphous coatings, Corros. Sci. 59 (2012) 10–19, https://doi.org/10.1016/j.corsci.2012.02.003.
[81] P.J. Cumpson, The Thickogram: a method for easy film thickness measurement in XPS, Surf. Interface Anal. 29 (2000) 403–406, https://doi.org/10.1002/1096-9918(200006)29:6<403::AID-SIA884>3.0.CO;2-8.
[82] E. Gardin, S. Zanna, A. Seyeux, A. Allion-Maurer, P. Marcus, Comparative study of the surface oxide films on lean duplex and corresponding single phase stainless steels by XPS and ToF-SIMS, Corros. Sci. 143 (2018) 403–413, https://doi.org/10.1016/j.corsci.2018.08.009.
[83] S. Tanuma, C.J. Powell, D.R. Penn, Calculations of electron inelastic mean free paths. IX. Data for 41 elemental solids over the 50 eV to 30 keV range, Surf. Interface Anal. 43 (2011) 689–713, https://doi.org/10.1002/sia.3522.
[84] Z. Li, C. Zhang, L. Liu, Wear behavior and corrosion properties of Fe-based thin film metallic glasses, J. Alloy. Compd. 650 (2015) 127–135, https://doi.org/10.1016/j.jallcom.2015.07.256.
[85] A. Kumar, S.K. Nayak, K. Sarkar, A. Banerjee, K. Mondal, T. Laha, Investigation of nano- and micro-scale structural evolution and resulting corrosion resistance in plasma sprayed Fe-based (Fe-Cr-B-C-P) amorphous coatings, Surf. Coat. Technol. 397 (2020) 126058, https://doi.org/10.1016/j.surfcoat.2020.126058.
[86] H.J.T. Ellingham, Transactions and Communications, J. Soc. Chem. Ind. 63 (1944) 125–160, https://doi.org/10.1002/jctb.5000630501.
[87] A. Chyrkin, Oxidation induced phase transformations and lifetime limits of chromia forming nickel base alloy 625, M.S. Thesis, RWTH, Aachen, n.d. ⟨https://publications.rwth-aachen.de/record/82719/files/4248.pdf%0A⟩.
[88] M.V. Glazoff, S.N. Rashkeev, J.S. Herring, Controlling chromium vaporization from interconnects with nickel coatings in solid oxide devices, Int. J. Hydrog. Energy 39 (2014) 15031–15038, https://doi.org/10.1016/j.ijhydene.2014.07.023.
[89] Roger W. Welker, Chapter 4 - Size analysis and identification of particles, in: Rajiv Kohli, K.L. Mittal. (Eds.), Dev. Surf. Contam. Clean. (2012) 179–213, https://doi.org/10.1016/B978–1-4377–7883-0.00004–3.
[90] C. Zhang, K.C. Chan, Y. Wu, L. Liu, Pitting initiation in Fe-based amorphous coatings, Acta Mater. 60 (2012) 4152–4159, https://doi.org/10.1016/j.actamat.2012.04.005.
[91] J.E. Berger, A.M. Jorge, G.Y. Koga, V. Roche, C.S. Kiminami, C. Bolfarini, W. J. Botta, Influence of chromium concentration and partial crystallization on the corrosion resistance of FeCrNiB amorphous alloys, Mater. Charact. 179 (2021) 111369, https://doi.org/10.1016/j.matchar.2021.111369.
[92] W.J. Botta, J.E. Berger, C.S. Kiminami, V. Roche, R.P. Nogueira, C. Bolfarini, Corrosion resistance of Fe-based amorphous alloys, J. Alloy. Compd. 586 (2014) S105–S110, https://doi.org/10.1016/j.jallcom.2012.12.130.